Thermal evolution and differentiation of planetesimals and planetary embryos

Ondřej Šrámek [a,b,*], Laura Milelli [c], Yanick Ricard [d], Stéphane Labrosse [d,e]

[a] University of Colorado at Boulder, Department of Physics, 390 UCB, Boulder, CO 80303, USA
[b] Department of Geophysics, Faculty of Mathematics and Physics, Charles University in Prague, V Holešovičkách 2, 18000 Praha, Czech Republic
[c] Institut de Physique du Globe-Sorbonne Paris Cité, Université Paris Diderot, UMR CNRS 7154, 1 rue Jussieu, 75238 Paris Cedex 05, France
[d] Laboratoire de Géologie de Lyon, CNRS, Université de Lyon 1, École normale supérieure de Lyon, 46 allée d'Italie, F-69364 Lyon Cedex 07, France
[e] Institut Universitaire de France, France

ABSTRACT

In early Solar System during the runaway growth stage of planetary formation, the distribution of planetary bodies progressively evolved from a large number of planetesimals to a smaller number of objects with a few dominant embryos. Here, we study the possible thermal and compositional evolution of these planetesimals and planetary embryos in a series of models with increasing complexities. We show that the heating stages of planetesimals by the radioactive decay of now extinct isotopes (in particular ^{26}Al) and by impact heating can occur in two stages or simultaneously. Depending on the accretion rate, melting occurs from the center outward, in a shallow outer shell progressing inward, or in the two locations. We discuss the regime domains of these situations and show that the exponent β that controls the planetary growth rate $\dot{R} \propto R^{\beta}$ of planetesimals plays a crucial role. For a given terminal radius and accretion duration, the increase of β maintains the planetesimals very small until the end of accretion, and therefore allows radioactive heating to be radiated away before a large mass can be accreted. To melt the center of ∼500 km planetesimal during its runaway growth stage, with the value $\beta = 2$ predicted by astrophysicists, it needs to be formed within a couple of million years after condensation of the first solids. We then develop a multiphase model where the phase changes and phase separations by compaction are taken into account in 1-D spherical geometry. Our model handles simultaneously metal and silicates in both solid and liquid states. The segregation of the protocore decreases the efficiency of radiogenic heating by confining the ^{26}Al in the outer silicate shell. Various types of planetesimals partly differentiated and sometimes differentiated in multiple metal–silicate layers can be obtained.

© 2011 Elsevier Inc. All rights reserved.

1. Introduction

Evidence from ^{182}Hf–^{182}W systematics of meteoritic samples points to a rapid accretion of terrestrial planetary bodies and their early differentiation into a metallic core and silicate mantle (Kleine et al., 2002; Yin et al., 2002). This applies not only to present-day planets but also to smaller bodies, a prime example being asteroid Vesta (e.g., Ruzicka et al., 1997). The inferred differentiation timescales for the parent bodies of some magmatic iron meteorites are as low as ∼1 My after the crystallization of CAIs (Kleine et al., 2009). Such a rapid differentiation most likely required a separation of metal from silicates in a partially or fully molten state. This could be accomplished by percolation of molten iron through solid silicates or by liquid–liquid separation in an early magma ocean, and most likely occurred by both mechanisms over different time windows (Stevenson, 1990).

The two important sources of energy in the early Solar System during planetesimal growth are radioactive heating by short-lived radionuclides and accretion heat brought by impacts. The former heat source is important for small growing bodies when the impact heating is still insignificant, within a few half-lives of the decaying radionuclides. The impact heating becomes the dominant energy source later as the planetesimal becomes more massive, and after the radionuclides have sufficiently decayed.

Separation of the denser molten metal from a porous silicate matrix may occur at temperatures in between the melting temperature of the metallic phase and the silicate solidus. Static percolation theory relates permeability at small melt fraction to the magnitude of dihedral angle formed between liquid metal and solid silicate grains (e.g., von Bargen and Waff, 1986). For a dihedral angle below the critical value of 60° an interconnected network of melt tubules are formed and porous flow is possible even for tiny melt fractions. On the other hand, in the case of larger angles, the melt tends to form isolated drops and a minimum melt fraction is necessary to get interconnection. For this reason, this issue has been the focus of many experimental studies. At high pressure,

* Corresponding author at: University of Colorado at Boulder, Department of Physics, 390 UCB, Boulder, CO 80303, USA.
E-mail address: ondrej.sramek@colorado.edu (O. Šrámek).

large dihedral angles have been found (Minarik et al., 1996; Shannon and Agee, 1996; Terasaki et al., 2005) and percolation was generally considered as an inefficient core formation mechanism. However, recent experimental results of Terasaki et al. (2008) suggest that dihedral angles fall below 60° at conditions of high oxygen fugacity and pressures below 2–3 GPa, and percolation may thus be the dominant segregation mechanism in planetary bodies with a radius less than ~1300 km. Moreover, even for angles above the critical value, the threshold for connectivity has been constrained from *in situ* electrical conductivity measurements (Yoshino et al., 2003, 2004; Roberts et al., 2007) to be 3–6 vol.%, even though some studies put the threshold higher (Walte et al., 2007; Bagdassarov et al., 2009). In any case, the typical reduced metal content of chondrites (up to 8% by volume for ordinary chondrites and even higher for some carbonaceous, enstatite and other chondrites; e.g., Krot et al., 2003; Scott and Krot, 2003), is above this threshold and the total metal content that forms planetary cores, about 20% by volume, is well above this threshold. Once the interconnectivity is established, the liquid iron can separate by percolation and its volume fraction decreases down to a "pinch-off" fraction, which is somewhat smaller than the percolation threshold (von Bargen and Waff, 1986; Terasaki et al., 2005).

Another aspect of the problem that has been completely left out of the discussion up to now concerns the deformation of the solid matrix. Indeed, even if permeability is sufficient to allow for Darcy flow with in- and out-flow, the situation is quite different in the case of a fixed volume. For the metal to go down and form the core, the partially solid silicate matrix needs to move up and therefore deform viscously, a process termed compaction. The high viscosity of the solid matrix can be the main limiting factor for core formation in planetesimals particularly at high permeability. Some early experiments (Takahashi, 1983; Walker and Agee, 1988) of partial melting of meteorites did not observe metal migration, which was interpreted as indication for the necessity of silicate melting (Taylor, 1992). However, the main reason is that compaction at that scale is very difficult to achieve even when the metal network is well connected. A crude estimate of the timescale for phase separation by this process can be obtained by balancing the available gravitational deviatoric stress $\Delta\rho gd$, with $\Delta\rho \sim 5000$ kg m^{-3} being the density difference between metal and silicate, g the acceleration of gravity and d the length-scale at which the process must occur, and the viscous resistance of the matrix, $\eta v/d = \eta/t$, with $\eta \sim 10^{18}$ Pa s the silicate viscosity, v the velocity of its deformation and t the timescale. For a laboratory experiment, where $d \sim 1$ cm and $g = 10$ m s^{-2}, one gets $t = \eta/(\Delta\rho g\ d) \sim 100$ My whereas for a planetesimal where $d \sim 500$ km and $g \sim 1$ m s^{-2}, $t \sim 10$ yr. This explains well why segregation of metal through a deforming solid matrix under Earth gravity is not possible to observe in the laboratory but is a viable mechanism for planetesimals.

In order to establish whether the melting temperature of the metallic component can be reached in a planetesimal, various authors considered ^{26}Al and ^{60}Fe heating of an instantaneously

formed planetesimal (e.g., Yoshino et al., 2003; Walter and Tronnes, 2004; Rubie et al., 2007). They concluded that planetesimals of radius larger than ~30 km experienced significant melting of the metallic component. However, as Merk et al. (2002) showed using models where the planetesimal radius increases linearly with time, the assumption of instantaneous formation at its final size is a crucial limiting factor in this analysis. The maximum temperature reached in the planetesimal's interior depends strongly on the accretion model. In order to properly constrain the thermal evolution of a planetesimal, one must consider the interplay between the accretion rate, generally variable in time, the final accreted size, and the possible delay of accretion after the element synthesis in the solar nebula.

In this study we investigate the thermal evolution of accreting planetesimals and planetary embryos (the continuous evolution described in the paper, from small to large bodies, makes it difficult to use a strict vocabulary, and we use loosely and interchangeably the terms planetesimal and embryo). In particular, we explore the effect of different choices for the accretion law, and the time interval over which accretion occurred. Unlike Merk et al. (2002), we include the thermal and gravitational energies brought by the impactors responsible for the growth of the planetesimal and employ a multiphase model that accounts for the separation of the metal from the silicates.

The sequence of models is constructed from the simplest scenario, i.e., a volumetrically-heated fixed-radius body with no differentiation, to more realistic cases. This way, the effects that various physical aspects of the final model have on the thermal evolution can be shown and discussed individually.

2. Thermal evolution without differentiation

2.1. Fixed radius, ^{26}Al heating

As a first estimate of planetesimal temperatures we consider a body of fixed radius heated by short-lived radionuclides. At this point we do not consider the accretion of the planetesimal or the segregation of metal. The thermal evolution is controlled by diffusion, heat production, $H(t)$ (in W kg^{-1}), and potentially latent heat release Q_L. The temperature $T(r, t)$ in the spherically symmetric body follows:

$$\overline{\rho C}\frac{\partial T}{\partial t} + Q_L = \frac{1}{r^2}\frac{\partial}{\partial r}\left(\overline{k_T}r^2\frac{\partial T}{\partial r}\right) + \overline{\rho H(t)}, \tag{1}$$

where t is time and r is the radial coordinate. We start with a simple homogeneous mixture of silicate material and metal. The volumetric heat capacity $\overline{\rho C}$, the thermal conductivity $\overline{k_T}$ and heat sources $\overline{\rho H(t)}$ are calculated as volume fraction-weighted averages of the respective metal and silicate values (e.g., $\overline{k_T} = k_T^{met}\phi + k_T^{sil}(1-\phi)$ where ϕ is the volume fraction of metal, considered to be 18%). The important nuclides are ^{26}Al with half-life $\tau_{1/2}^{Al} = 0.717$ My

Table 1
The initial heat production (at CAI formation time) for each radionuclide, H_0^{Al} and H_0^{Fe}, is calculated from $H_0 = \mathcal{C}\mathcal{F}N_A\lambda\mathcal{E}/\mathcal{M}$. $\mathcal{C}$ is the chondritic weight fraction of the element (Lodders and Fegley, 1998), $\mathcal{F}$ is the initial (CAI) isotopic ratio (fraction of radionuclide for element; Huss et al., 2009; Ouellette et al., 2009), $\mathcal{E}$ is the nuclear decay energy per atom (Castillo-Rogez et al., 2009), $\lambda = (\ln 2)/\tau_{1/2}$ is the decay constant, $\mathcal{M}$ is the molar mass, and $N_A = 6.022 \times 10^{23}$ is Avogadro's number.

Quantity	Symbol	Unit	Al, ^{26}Al values	Fe, ^{60}Fe values
Chondritic abundance (element/chondrite)	$\mathcal{C}$	kg/kg	0.00865	0.182
Initial isotopic fraction (^{rad}X/X where X is Al or Fe)	$\mathcal{F}$	N/N	5×10^{-5}	$(3–10) \times 10^{-7}$
Molar mass of radionuclide	$\mathcal{M}$	kg mol^{-1}	0.026	0.060
Half-life of radionuclide	$\tau_{1/2}$	My	0.74	2.62
Decay energy	$\mathcal{E}$	J/atom	5.1×10^{-13}	4.3×10^{-13}
Decay constant	$\lambda = \frac{\ln 2}{\tau_{1/2}}$	s^{-1}	3.0×10^{-14}	1.5×10^{-14}
Initial radiogenic heat production (W kg^{-1} chondrite)	$H_0 = \frac{\mathcal{C}\mathcal{F}N_A\lambda\mathcal{E}}{\mathcal{M}}$	W kg^{-1}	1.5×10^{-7}	$(0.3–1.2) \times 10^{-8}$

Table 2

Parameter values. Thermal expansion and the temperature dependence of specific heat, thermal conductivity and viscosity are neglected for both the silicate and the metal. The permeability coefficient assumes a characteristic silicate matrix grain size of 1 mm.

Quantity	Symbol	Value	Unit
Density of metal	ρ^{met}	7800	kg m^{-3}
Density of silicate	ρ^{sil}	3200	kg m^{-3}
Specific heat of metal	C^{met}	450	J K^{-1} kg^{-1}
Specific heat of silicate	C^{sil}	1200	J K^{-1} kg^{-1}
Latent heat of metal	L^{met}	250	kJ kg^{-1}
Latent heat of silicate	L^{sil}	500	kJ kg^{-1}
Melting temperature of metal	T_m^{met}	1261	K
Melting temperature of silicate	T_m^{sil}	1408	K
Temperature of solar nebula	T_{neb}	300	K
Viscosity of solid phase	μ_m	10^{18}	Pa s
Viscosity of liquid metal	μ_f	1	Pa s
Thermal conductivity of metal	k_T^{met}	50	W m^{-1} K^{-1}
Thermal conductivity of silicate	k_T^{sil}	3	W m^{-1} K^{-1}
Permeability coefficient	k_0	4.4×10^{-9}	m^2
Permeability exponent	n	2	
Initial metal volume fraction	ϕ_0	0.18	

(http://www.nucleide.org/) and ^{60}Fe whose half-life has been recently reevaluated to $\tau_{1/2}^{Fe} = 2.62$ My (Rugel et al., 2009). The numerical values are listed in Table 1. Because of recently revealed uncertainties about the initial abundance of ^{60}Fe (Quitté et al., 2010), we do not consider heating by this nuclide and therefore $\overline{\rho H(t)} = \bar{\rho} H_0^{Al} 2^{-t/\tau_{1/2}^{Al}}$. We also neglect the temperature dependence of specific heat – even though C should be decreased at low temperature according to the Debye model (Merk et al., 2002); this is a minor effect. The parameter values are summarized in Table 2.

Without solving Eq. (1), it is clear that for planetesimal radius R smaller than the diffusion length $\pi\sqrt{\kappa\tau_{1/2}} \approx 20$ km (the thermal diffusivity is $\kappa = \overline{k_T}/\overline{\rho C}$) the maximum temperature reached at the center is controlled by diffusion and, varies with time as $\Delta T \sim H(t)R^2/(6\kappa C)$. As an example, for a 1-km size planetesimal the maximum temperature increase is only 9 K; for a 5 km planetesimal the maximum temperature increase is 220 K. On the contrary, a large planetesimal for which thermal diffusion is negligible, reaches a final internal temperature of $\Delta T \sim H(0)\tau_{1/2}/(C\ln 2)$ (5300 K with values from Table 1). These simple estimates already show that up to the kilometer scale, planetesimals are unaffected by the initial radioactivity, while larger bodies that have accreted rapidly reach their melting temperature quite easily. For the sake of simplicity, the melting of each component is assumed univariant and we use $T_m^{met} = 1261$ K for the metal eutectic temperature (Fei et al., 1997) and $T_m^{sil} = 1408$ K for the silicate solidus (Jurewicz et al., 1993) (see Table 2). We also consider that the densities of metal and silicate do dot change during melting. With the iron abundance of 18 wt.%, and the latent heat $L^{met} = 250$ kJ kg^{-1} for the metal and $L^{sil} = 500$ kJ kg^{-1} for the silicates (Kojitani and Akaogi, 1995) (Table 2), the melting of the entire metal content consumes the energy equivalent to a temperature decrease of 42 K, and the melting of the silicates requires the heat equivalent to a 390 K temperature drop.

We solve Eq. (1) numerically using finite differences with equidistant spacing in r. The time evolution uses Crank–Nicholson semi-implicit scheme, which leads to an inversion of a tridiagonal matrix at each time step. To account for the latent heat exchanges, we monitor the proportions of solid metal and silicates and use a simple form of the enthalpy method. We compute a first estimate of the temperature; if larger than the melting temperature of either the metal or the silicates, we decrease the temperature to the appropriate melting conditions and the corresponding proportion of the solid phase whose melting has provided the necessary enthalpy, until complete exhaustion.
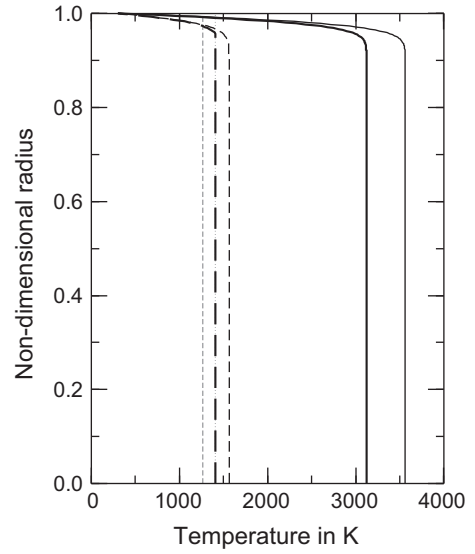

Fig. 1. Temperature as function of normalized radius for a 500 km planetesimal, 1 My after its instantaneous formation. Planetesimal formation offset from the time of element synthesis t_0 is 0 (solid line) and 1 My (dashed line). When the latent heat of metal and silicate are neglected, higher temperatures are reached (thin solid and dashed lines). The melting temperature of metal and silicates are depicted by dotted lines.

Fig. 1 depicts the solution of Eq. (1) for a planetesimal of a fixed radius $R = 500$ km heated purely by ^{26}Al at time 1 My (Fig. 1, solid line). The initial and surface temperature are set to the ambient temperature of the nebula T_{neb}; we use $T_{neb} = 300$ K which is an upper bound of the reasonable range of 200–300 K for the nebula temperature (Ghosh and McSween, 1998; Cohen and Coker, 2000). The interior of the planetesimal is isothermal and the temperature falls off within a boundary layer of thickness increasing with time as $\sqrt{\kappa t}$. The plateaus corresponding to the coexistence of solid and liquid phases of metal and silicates at their respective melting temperatures are very narrow and not really visible on this figure. Without latent heat, the internal temperature would increase by 430 K (thin solid line).

If planetesimals are formed at time t_0 relative to the Ca–Al-rich inclusions, their radioactive sources are already reduced by $2^{-t_0/\tau_{1/2}}$. For an instantaneous planetary formation postponed by $t_0 = 1$ My (dashed line) the peak temperature is reduced by factors of 2 and is buffered at the silicate melting temperature (all the metal and 25% of the silicates are molten). The case without latent heat (thin dashed line) is shown for comparison. This basic calculation illustrates the relationship between Solar System early chronology and the geophysical evolution of planetesimals.

2.2. Effect of accretion

Of course, the planetesimal does not reach a finite radius instantaneously. We define its accretion rate $dR/dt \equiv \dot{R}$. To solve the diffusion Eq. (1) for the growing planet we perform a change of variables and define $u(r,t) = r/R(t)$; u will stay bound between 0 and 1 throughout the planetesimal growth. The rules of differentiation lead to

$$\overline{\rho C}\left(\frac{\partial T}{\partial t} - u\frac{\dot{R}}{R}\frac{\partial T}{\partial u}\right) + Q_L = \frac{1}{u^2}\frac{\partial}{\partial u}\left(\frac{\overline{k_T}}{R^2}u^2\frac{\partial T}{\partial u}\right) + \overline{\rho H(t)}. \quad (2)$$

In this stretching reference frame the effective diffusivity decreases with the square of the planetary size, while the accretion on the planetary surface gives rise to an advection term transporting the isotherms towards the center.

The accretion of Solar System bodies becomes dominated by gravitational accumulation when the mass of individual small planetesimals in the protoplanetary disc reaches 10^9–10^{15} kg corresponding to ~0.1–10 km size; first a runaway growth occurs, later followed by oligarchic growth toward planetary embryos (see a review by Kortenkamp et al. (2000) and references therein). The evolution of the dominant planetary body's mass can be written as

$$\frac{1}{M}\frac{dM}{dt} \propto M^{\alpha}, \quad \text{or} \quad \dot{R} \propto R^{\beta}. \tag{3}$$

Eq. (3) describes the growth from an initial small nucleus of a non-zero radius, typically few km, which represents the lower limit where gravitational attraction becomes the primary driving mechanism for planetesimal growth. Below this stage, the process by which grain dusts collide and stick together remains an unsolved problem, even though models that may overcome this difficulty were recently proposed (Johansen et al., 2007; Cuzzi et al., 2008; see also Morbidelli et al., 2009).

During the initial runaway growth stage where a single dominant body within an orbital region grows much faster that other objects, the exponent α is about 1/3 and thus $\beta = 3\alpha + 1 = 2$; during the later oligarchic growth of several embryos of comparable size located at different orbital zones, α is about $-1/3$, thus $\beta = 0$ (e.g., Kortenkamp et al., 2000). The value of the exponent β affects drastically the temperature profile in the planetesimals compared to the case of instantaneous accretion. The higher the exponent β, the longer the planetesimal remains small relative to the diffusion length scale, and the more efficiently the initial radiogenic heat can be diffused away. We will show cases where we keep the exponent β constant for the duration of the simulations, but we vary its value within the bounds discussed above. The timescale of protoplanet growth is ~0.7 My at 1 AU and increases with orbital distance, e.g., reaches ~40 My at 5 AU (Kokubo and Ida, 2000).

The N-body simulations of gravitationally driven accretion (e.g., Kokubo and Ida, 2000) are usually started from a relatively large size bodies (10^{20} kg) because of computational limitations of this modeling. However, there is a good agreement between N-body simulations, and other approaches such as statistical simulations (e.g., Wetherill and Stewart, 1993) and multi-zone hybrid models (e.g., Weidenschilling et al., 1997) where the latter techniques consider the appropriate initial distribution of bodies of ~1 km

size. The exact choice of the initial radius has some quantitative effect on the results of our calculations (e.g., the maximum temperatures reached), especially in cases with large exponent β, where a larger initial radius leads to somewhat higher peak temperature. For example, this difference can reach few hundred K at most between cases started from a 1 km and 5 km seed, respectively. As the effect of initial radius is rather trivial, we will not discuss it further. In all our calculations we simply use the same initial radius of 5 km; note that this is much smaller than the diffusion length scale of 20 km discussed previously, so that the initial temperature remains close to that of the nebula. We also neglect the delay time between the condensation of the first CAI and the formation of the nucleus that we use to start the accretion model. This maximizes the heat production as some ^{26}Al had already decayed during this time.

In Fig. 2 we show the thermal structure at the end of the accretion period of a planetesimal that has grown to a final radius of 500 km over a period $t_a = 1$ My (Fig. 2a) and 5 My (Fig. 2b). We choose $\beta = 0$ (i.e., a constant radial growth rate relevant to oligarchic growth, dot-dashed-line line), $\beta = 1$ (an exponential growth rate, dashed line), and $\beta = 2$ (which is close to the value suggested by Kokubo and Ida (2000) for the super-exponential runaway growth, solid line). Here we assume that the material added at the surface has the ambient nebula temperature T_{neb}. The temperature profiles are very different from the previous case (cf. Fig. 1). Taking the accretion into account, only the oldest, central part of the planetesimal experienced important heating by short-lived radionuclides. The outer layers accrete after the ^{26}Al heating rate has significantly decreased. The maximum temperatures reached at the center by the end of accretion are much lower than in the case of instantaneous planetesimal formation in Fig. 1, especially for accelerated radial growth ($\beta = 1$ and 2). The temperature plateaus due to iron and silicate melting are clearly visible. For accretion duration $t_a = 1$ My, comparable to ^{26}Al half-file, significant radiogenic heating continues after the accretion period and the peak interior temperatures, reached around $t = 4$–5 My, amount to 4700 K, 3300 K and 2200 K for $\beta = 0$, 1 and 2, respectively. This late heating explains that for $\beta = 0$, larger temperatures are attained in Fig. 2b after 5 My of slow accretion. For what concerns the maximum temperature, a β of 2 is thus equivalent to delay the accretion by 1 My (see Fig. 1). For a large β and a slow accretion, the embryos do not melt.
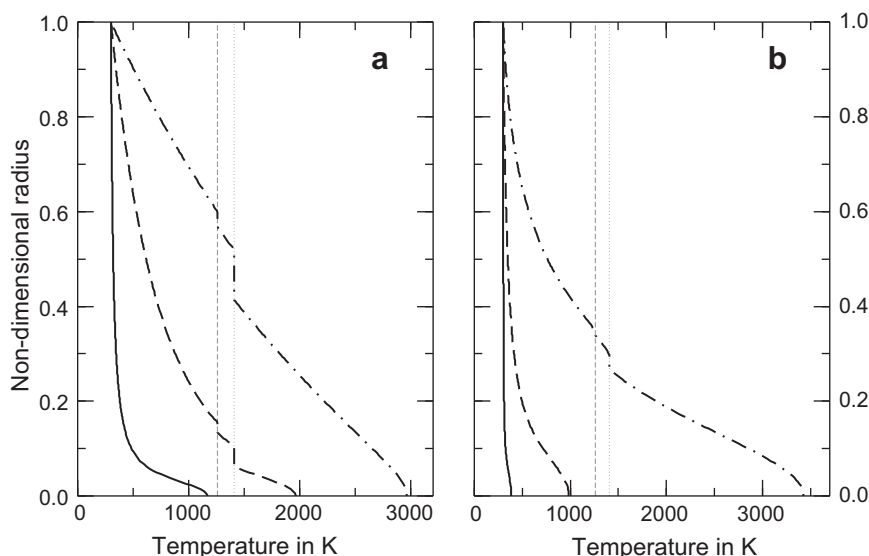

Fig. 2. Temperature as function of normalized radius for a planetesimal that has grown from an initial radius 5 km to its final radius 500 km over (a) 1 My and (b) 5 My immediately after the element synthesis. The exponent β in the growth rate law is 0 (dot-dashed line), 1 (dashed line), and 2 (solid line).

2.3. Heating by surface impacts

The planetary body grows by impacts and the impactors bring gravitational energy as well as thermal energy to the impacted planet. Both of these energies were neglected in Merk et al. (2002). Assuming that the impact velocity is equal to the escape velocity of the planet (certainly a very crude estimate which neglects a possible non-zero approach velocity of the impactor), an impactor of mass dm_{imp} brings gravitational energy $dE_g = (GM/R)dm_{imp}$ where $M = (4/3)\pi\bar{\rho}R^3$ is the mass of the target. The impacting bodies add to the target mass, therefore $dm_{imp}/dt = dM/dt = 4\pi\bar{\rho}R^2\dot{R}$, and the gravitational energy delivered per unit time amounts to

$$\frac{dE_g}{dt} = \frac{16}{3}\pi^2 G\bar{\rho}^2 R^4 \dot{R}. \tag{4}$$

(Solomon, 1979; Ricard et al., 2009). The thermal energy delivered is

$$\frac{dE_t}{dt} = 4\pi\bar{\rho}\overline{C}(T_{imp} - T_{neb})R^2\dot{R}, \tag{5}$$

where T_{imp} is the average temperature of the impactor. T_{imp} should clearly be smaller than (or at most equal to) the average temperature of the target, as by definition the impactor is less massive than the target, and therefore has diffused out its heat more efficiently. The different R-dependence of these two energy supplies indicates that large planets (e.g., $R > 900$ km, assuming $T_{imp} = 1000$ K) are mostly heated by deposition of gravitational energy, while the thermal energy of impactors is dominant for small planets.

The energy influx of impacts can either be radiated away from the surface or buried inside the planet. The thermal deposition at depth is due to the penetration of the impactor inside the planet and the propagation of a shock wave, while excavation and subsequent deposition of ejecta during impact heats the near-surface layer (Melosh, 1996; Senshu et al., 2002). Impact modeling suggests that a fraction $f = 20$–40% of the impactor kinetic energy is converted to thermal energy while the rest is radiated into space (e.g., O'Keefe and Ahrens, 1977). This proportion may be somewhat reduced for highly oblique impacts (e.g., Smither and Ahrens, 1991). The radiated heat controls the surface temperature according to the black body law, which gives

$$4\pi R^2\sigma(T^4 - T_{neb}^4) = -4\pi R^2 k_T\left.\frac{\partial T}{\partial r}\right|_{r=R} + (1-f)\left(\frac{dE_g}{dt} + \frac{dE_t}{dt}\right), \tag{6}$$

where σ is the Stefan–Boltzmann constant (possibly multiplied by an empirical emissivity that also includes the effect of the atmosphere; Carslaw and Jaeger, 1959; Ghosh and McSween, 1998). The heat diffusion at the surface, from the hot center of the planetesimal can also be neglected compared to the energy brought by the impacts. This equation provides therefore a direct estimate of the surface temperature of the planetesimal. As Matsui and Abe (1986) show, the blanketing effect of a volatile-rich primordial atmosphere tends to provide an insulating layer that prevents efficient radiation of heat into space. This blanketing effect, however, is probably negligible for the small planetesimals we consider.

Eq. (6) shows that the surface temperature necessary to radiate all the accretion heat is always very small. If a planetesimal grows to 500 km in 5 My while radiating heat, its surface temperature would only increase by 1, 3 or 50 K, for the three different exponents considered in the accretion law (3) (i.e., $\beta = 0$, 1 or 2, and maximizing the thermal energy input by assuming that the impactor has the average temperature of the target).

When the impact energy is deposited by a shock wave, the maximum depth of deposition is larger but comparable to the size of the impactor (Croft, 1982). Assuming that the impact energy is deposited uniformly over a depth ΔR, the burial of the impact energy is then equivalent to an internal heat source H_g, defined by

$$4\pi\bar{\rho}H_g R^2 \Delta R \sim f\left(\frac{dE_g}{dt} + \frac{dE_t}{dt}\right). \tag{7}$$

The energy burial in a shallow layer is an efficient mechanism to raise the planet's temperature. During the runaway growth, the number n of planetesimals of mass between m and $m + dm$ is $n \propto m^{-p}$ with $p \approx 2.5$ (e.g., Kokubo and Ida, 1996). From this distribution, the average size of an impactor hitting a planetary embryo of size R is found of order $R/5$ (obtained for $p = 2.7$). We use a burial depth proportional to the target radius and thus choose $\Delta R = R/5$. Keeping $\Delta R/R$ constant means that the mass ratio of the runaway protoplanet to the average body in the planetesimal system increases with time, in accordance with the results of planetary accretion modeling. In the case of steady growth (constant $\dot{R}$), the temperature increase is independent of $\dot{R}$ (H_g being proportional to $\dot{R}/\Delta R$, but acting during a time proportional to $\Delta R/\dot{R}$). It amounts to about 300 K for $R = 500$ km, $\Delta R = R/5$, $T_{imp} = 1000$ K and $f = 20\%$. For variable $\dot{R}$, and large exponent β in Eq. (3), larger impact heating are reached (see below).

In Fig. 3 we show the final temperature as function of radius for a planetesimal growing from a small seed to 500 km radius over $t_a = 1$ My, with the surface condition described as above and a fraction f of the impactor's gravitational and thermal energy is buried in a shallow layer of thickness $\Delta R = R/5$. Fig. 3a shows the temperature at the end of accretion with $f = 20\%$ for the three different accretion laws. Fig. 3b shows how the final temperature varies with the buried energy fraction f in the case of highly non-linear radial growth (accretion law exponent $\beta = 2$). As is clear from the plots, the near-surface energy burial increases the planetesimal interior temperature relative to the case with a simple isothermal surface condition, and can even result in a non-monotonic thermal profile, especially in the case of strongly accelerated radial growth ($\beta = 2$). The shallow-depth temperature increases by up to 350 K in the case with $f = 40\%$ and $\beta = 2$ (Fig. 3b).

2.4. Results without differentiation

We now investigate in a more systematic fashion how the thermal evolution of planetesimals varies as a function of the duration of accretion t_a, the accretion law (i.e., the value of exponent β in Eq. (3)) and the final size of the body R_f. We ran a series of numerical experiments where these parameters are varied. In each case the initial seed radius is 5 km and initial temperature T_{neb}. Only radiogenic heating by ^{26}Al is considered, and the accretion is supposed to start without delay after the element synthesis. Notice, however, that increasing the exponent β delays the start of substantial accretion – and thus plays a somewhat similar role for radiogenic heating as a delay between element synthesis and onset of accretion. The surface temperature is controlled by radiation, and ($f = 20\%$) of incoming gravitational energy is deposited in a shallow layer of thickness $R/5$ (see Section 2.3). No differentiation is yet considered even in the presence of molten phases.

In Fig. 4 we show the peak temperature T_{max} reached in the planetesimal (top row) and the maximum volumetric fraction of total metal + silicate melt (middle row), as functions of t_a and β. We also plot the time when peak temperature is reached as a function of the accretion period t_a (bottom row). The results are shown for planetary embryos with terminal radii 500 km (left column), 1000 km (middle column) and 1500 km (right column).

Generally, the peak temperature (Fig. 4a–c) is sensitive to both the accretion history (β) and the duration of the accretion (t_a). For $\beta \lesssim 1$ radiogenic heating dominates the heat sources, and T_{max} is mostly decreasing with β. A higher β means that the planetesimal remains relatively small, and therefore cools more efficiently at the earlier times, when short-lived radioactivity is most intense. The planetesimal temperatures decrease with increasing duration of
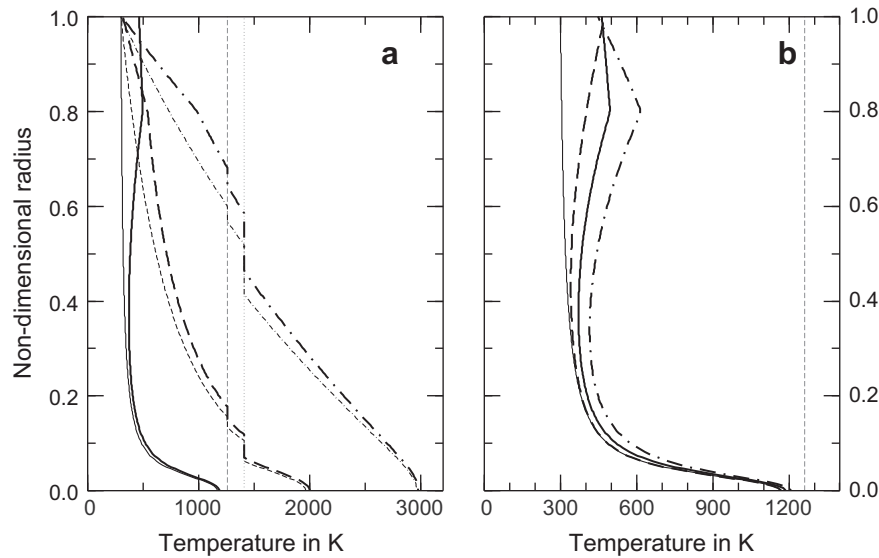
Fig. 3. Temperature as function of normalized radius for a planetesimal that has grown from 5 km radius to its final radius of 500 km over 1 My immediately after the element synthesis. The "black body radiation–energy burial" surface boundary condition with $\Delta R = R/5$ is used (see Section 2.3). (a) Calculated with $f = 20\%$ and the growth rate exponent $\beta = 0$ (dot-dashed), 1 (dashed) and 2 (solid). Corresponding curves for $f = 0$ and isothermal surface boundary condition are shown as thin lines. (b) Effect of varying the fraction of deposited energy f with $\beta = 2$. Curves for $f = 0\%$ (dashed), 20% (solid) and 40% (dot-dashed) are shown. The thin solid curve is for isothermal surface boundary condition (cf. Fig. 2).

accretion. At $\beta \gtrsim 2$, the mass accretes at the end and deposits a significant gravitational energy in a near surface shell. Only for large enough final size is this gravitational heating sufficient to bring the temperature above melting (Fig. 4c).

Increasing the final radius at unchanged t_a and β (i.e., going from panel a to panels b and c) results in higher interior temperatures, because of less efficient diffusive cooling as well as a stronger gravitational heating. Maximum temperatures in the explored parameter space amount to ~5000 K. They are reached either by intense heating due to short-lived radioactivity only (case $\beta = 0$ panels a, b or c) or by combined effect of radioactivity and impacts (case $\beta = 2.5$ when the final planetesimal radius is large, panel c).

The largest molten volume fraction of the planetesimal (Fig. 4d–f) is obtained when the duration of accretion is the shortest. It is relatively independent of the accretion law exponent β. Fast accretion ($t_a \lesssim 1$ My) results in essentially a fully molten planetesimal, while prolonged accretion ($t_a \gtrsim 3$ My) produces planetesimals with a small volumetric fraction of melt (few tens %). Here again, for large planetesimals or planetary embryos, surface heating becomes large and near-surface melting occurs (Fig. 4f).

In Fig. 4g–i, we depict the time when the maximum temperature is reached in the planetesimal. The shaded area depicts the domain where the peak temperature occurs during accretion. Maximum temperatures in the white area are reached in planetesimals after they stopped growing. The different symbols – red circles, green triangles and blue squares – correspond to $\beta = 0$, 1 and 2. Where filled, melting occurs. When the accretion interval t_a is shorter than 3.5–4 My (about $5 \times {}^{26}$Al half-life), the peak temperature is only reached after the accretion has completed. Only when the accretion interval exceeds 4 My, the maximum temperature is attained during the times when the planetesimal is still growing. The extensive melting observed in cases with fast accretion is therefore mainly caused by continued radiogenic heating in the post-accretion time. For $\beta = 2$ there are several cases where melting never occurs, which was already seen as blue areas in Fig. 4a–c.

For each of the three final radii (ranging from 500 km to 1500 km), we identify large regions in the t_a–β parameter space where the peak temperatures reach well above the liquidus of

the silicate phase, which indicates the formation not only of a protocore but also of a magma ocean. For smaller final radius and smaller β (illustrated in Fig. 5a, case with $R_f = 500$ km, $t_a = 3$ My and $\beta = 0$), the magma ocean forms at the center of the planetesimal and the magma ocean boundary extends outwards as the interior is further heated by the radioactive sources. The interior magma ocean can span a significant fraction of the total radius (Fig. 5a), or can be relatively small restrained to the very center of the planetesimal (Fig. 5b; case with $R_f = 500$ km, $t_a = 3$ My, $\beta = 1$). In Fig. 5a,b, a zoned structure forms with a totally molten central region, a layer of partially molten silicates and liquid metal, a layer of solid silicates and liquid metal in the temperature interval in between Fe–S eutectic and silicate solidus, a shell with partially molten metal in solid silicate matrix, and finally an entirely solid surface shell. The late-stage gravitational heating of the outer shell becomes significant for cases with accelerated growth. Fig. 5c shows a case with $R_f = 1500$ km, $t_a = 3$ My and $\beta = 1$ where both radiogenic and gravitational heating raise the temperature above melting in two distinct radial regions – in the center of the planetesimal and in a shell at shallow depth. When β is increased from 1 to 2, most of the radiogenic heat is lost by the time any significant growth of the body occurs while the gravitational heating becomes stronger during the very fast late growth. Only a near-surface, relatively thick magma ocean forms (Fig. 5d). The volumes of the protocores and the magma oceans that are formed during accretion are discussed later, when the differentiation processes are taken into account.

Fig. 6 shows a regime diagram of the peak temperature plot that summarizes the previous results. It shows schematically the four regions corresponding to:

- Deep melting due to radiogenic heating at low values of β.
- Shallow melting due to gravitational heating at large β; this domain increases in size with the terminal radius of the planetesimal, as shown by arrows.
- An overlap domain with both deep and shallow melting at intermediate values of β and shorter duration of accretion.
- A domain of no melting at intermediate β and long accretion duration, typically longer than 1–2 My.
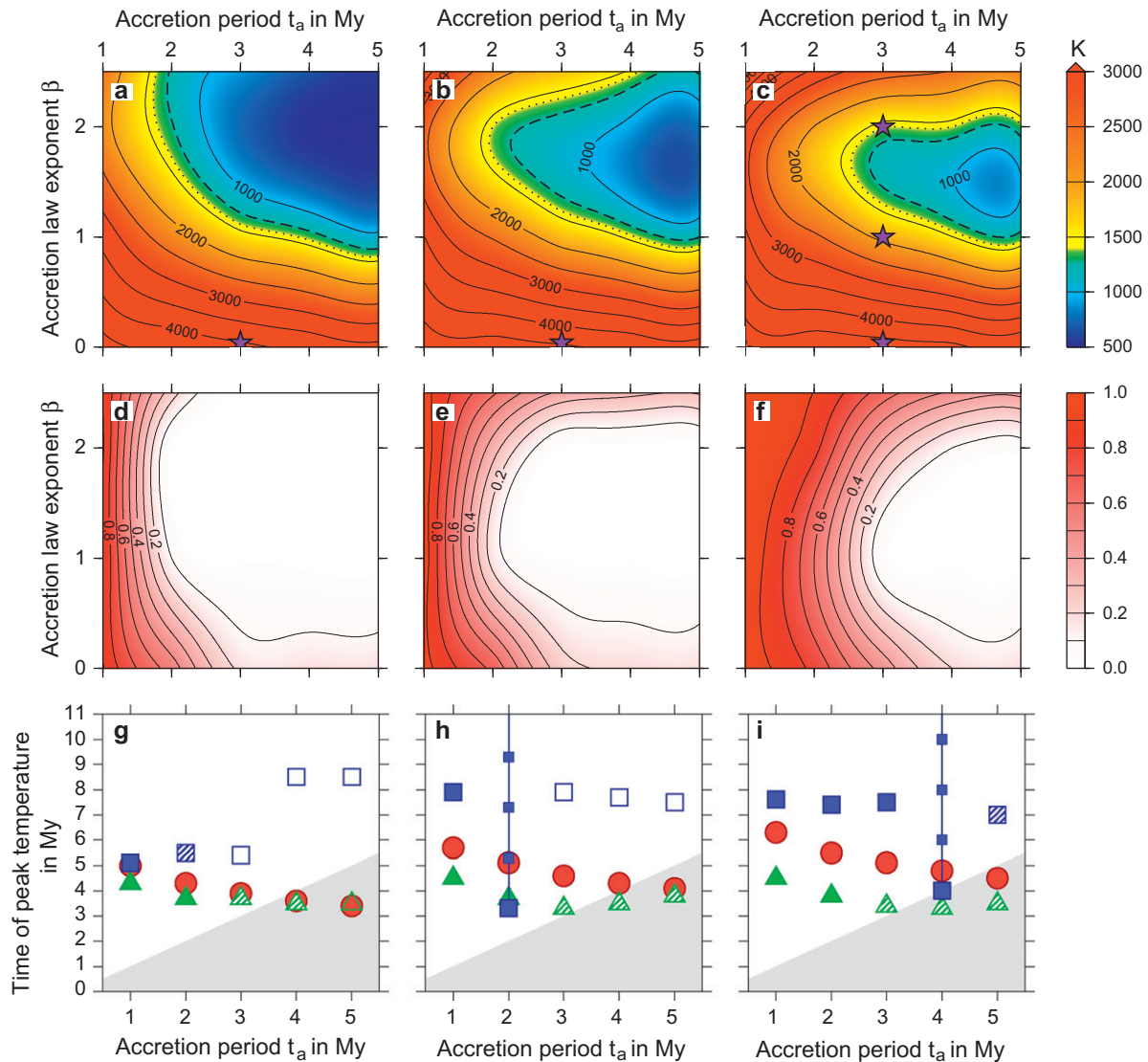
Fig. 4. (top row) Peak temperature and (middle row) maximum volume fraction of melt reached in the planetesimal as a function of accretion period duration t_a and accretion law (exponent β of Eq. (3)); (bottom row) time when peak temperature was reached as a function of accretion period t_a for a planetesimal with final radius R_f = 500 km. Shown for R_f = 500 km (left column), R_f = 1000 km (middle column) and R_f = 1500 km (right column). Accretion is assumed to begin immediately after the element synthesis (t_0 = 0). Thick dashed and dotted contours in a–c show the Fe–S eutectic temperature and the silicate solidus temperature, respectively. In g–i are shown cases with β = 0 (red circles), β = 1 (green triangles) and β = 2 (blue squares) with no melting (empty symbols), minute amount of melting (below 5 vol.%; hatched), and melting above 1 vol.% (filled). Vertical lines (in panels h and i) indicate peak temperature buffering at the melting temperature of the silicates. The stars in panels a–c give the positions of parameters for cases in Figs. 7–11. (For interpretation of the references to color in this figure legend, the reader is referred to the web version of this article.)

Various situations of melting are therefore possible. In some cases, a single mechanism is responsible for melting – either from the center outward due to radiogenic heating or in a near-surface shell due to surface impact heating. In other cases, the two mechanisms can act simultaneously. When the radial growth is strongly accelerated ($\beta \approx 2$), only planetesimals that grow rapidly ($t_a \lesssim 2$ My) to a large size ($R_f \gtrsim 500$ km) can melt significantly. This situation corresponds mostly to delaying the planetesimal formation until the last moment.

3. Thermal evolution with differentiation

So far we have only considered diffusive transfer of heat within the planetesimal, and have kept the spatial distribution of its major constituents uniform at all times. It is obvious, however, that as soon as melting occurs and viscosity dramatically decreases, the much heavier metal separates from the silicates. Differentiation will result in fractionation of heat producing elements – we assume that ^{26}Al is entirely carried by the silicate phase, which in turn will affect the thermal evolution.

Several mechanisms for metal–silicate separation have been proposed, namely the percolation of molten metal along an inter-connected network in deforming solid silicate frame, separation of molten metal from molten silicates in a magma ocean, and downward migration of large-scale metal-rich bodies in the form of diapirs or propagating fractures (e.g., Stevenson, 1981; Stevenson, 1990; Rubie et al., 2007; Golabek et al., 2008; Samuel and Tackley, 2008; Monteux et al., 2009; Ichikawa et al., 2010; King and Olson, 2011). With the present spherically symmetric (1-D) model we cannot address possible lateral variations in metal content (i.e., the diapir or large-scale fracture model; see Ricard et al., 2009; Šrámek et al., 2010). In any case, in small planetesimals, the large-scale diapirs and the propagating fractures should not be the
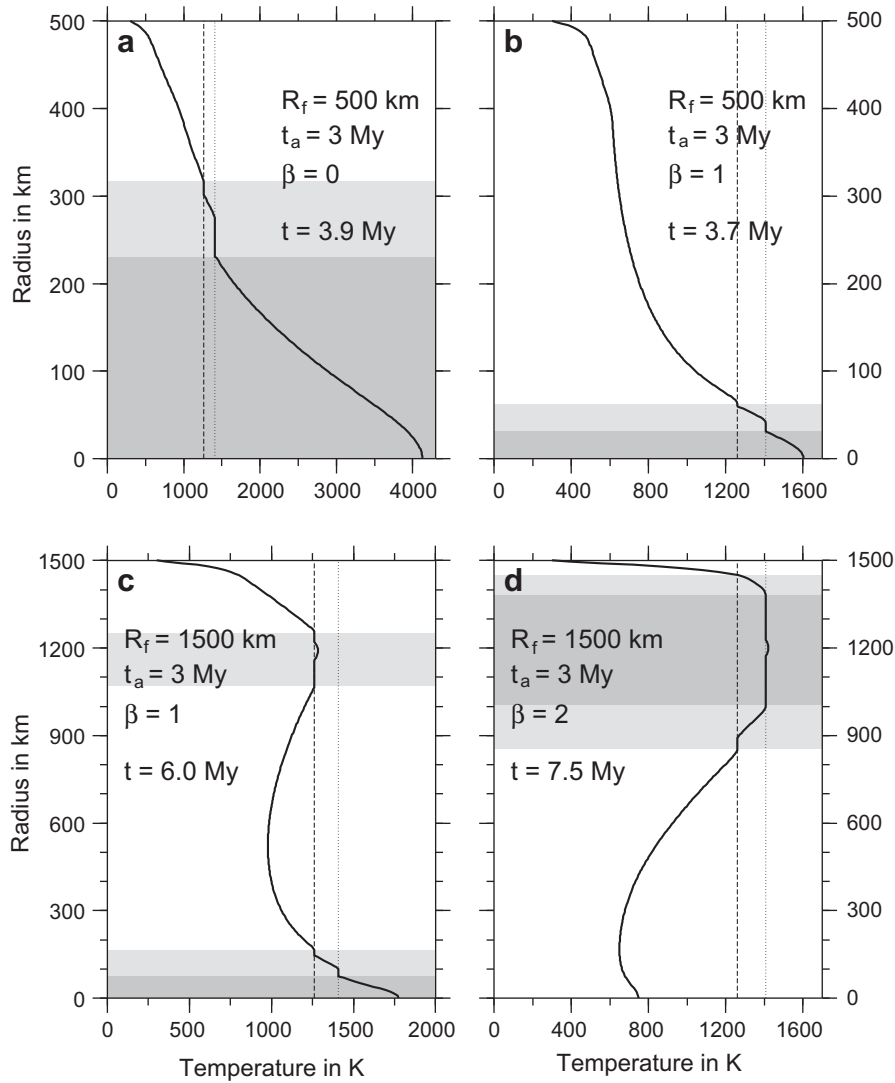
Fig. 5. Temperature as a function of radius at the time when the peak temperature was reached (solid line). Fe–S eutectic temperature and silicate solidus shown as thin dashed and dotted lines, respectively. Cases with (a) $R = 500$ km, $t_a = 3$ My, $\beta = 0$ at $t = 3.9$ My; (b) $R = 500$ km, $t_a = 3$ My, $\beta = 1$ at $t = 3.7$ My; (c) $R = 1500$ km, $t_a = 3$ My, $\beta = 1$ at $t = 6.0$ My; (d) $R = 1500$ km, $t_a = 3$ My, $\beta = 2$ at $t = 7.5$ My. In all cases $t_0 = 0$. Partially/totally molten regions are shown with lighter/darker shading.
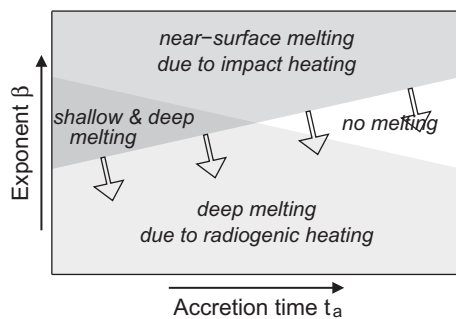

Fig. 6. Schematic of the regime diagram of peak temperatures in planetesimal. The white arrows show how the near-surface melting evolves with the terminal planetesimal size.

major mechanisms of metal silicate separation and we specifically study here the phase separation by compaction. Moreover, the diapir propagation first needs melting and phase separation in order to form the diapir itself and thus it occurs necessarily after percolation of the metal through compaction.

3.1. Multiphase model

We consider a medium containing four constituents: solid silicates, solid metal, liquid metal and liquid silicates. We use the superscripts *sil* and *met* to describe the silicate and the metal, and subscripts m and f to denote the solid *matrix*, and the molten *fluid*. Their respective volume fractions are ϕ_m^{sil}, ϕ_m^{met}, ϕ_f^{met} and ϕ_f^{sil}, the sum of which is 1:

$$\phi_m^{sil} + \phi_m^{met} + \phi_f^{met} + \phi_f^{sil} = 1. \tag{8}$$

We assume that when silicates and metal are both solid, they move at an identical velocity, the solid matrix $\mathbf{v}_m^{sil} = \mathbf{v}_m^{met} \equiv \mathbf{v}_m$, and are submitted to identical pressure fields $P_m^{sil} = P_m^{met} \equiv P_m$. The molten metal and molten silicates are submitted to pressure $P_f^{met} = P_f^{sil} \equiv P_f$ (we neglect the effect of interfacial tensions in the present model) but can move at different velocities $\mathbf{v}_f^{met}$ and $\mathbf{v}_f^{sil}$, so that separation from the solid is possible, as well as separation of liquid metal from liquid silicates. In thermodynamical sense there are two components – the metal and the silicates, and three phases: the solid "matrix" which is a mixture of silicates and metal, the molten metallic phase, and the molten silicates. Phase change

Table 3
Model constituents and corresponding variables and parameters.

Constituent	Solid silicates	Solid metal	Liquid metal	Liquid silicates
Volume fraction	ϕ_m^{sil}	ϕ_m^{met}	ϕ_f^{met}	ϕ_f^{sil}
Density	ρ^{sil}	ρ^{met}	ρ^{met}	ρ^{sil}
Specific heat	C^{sil}	C^{met}	C^{met}	C^{sil}
Phase	— Solid matrix —		Fluid	Fluid
Solid/liquid vol. frac.	$\phi_m = \phi_m^{sil} + \phi_m^{met}$		$\phi_f = \phi_f^{met} + \phi_f^{sil}$	
Viscosity	μ_m	μ_m	μ_f^{met}	μ_f^{sil}
Pressure	P_m	P_m	P_f	P_f
Velocity	$\mathbf{v}_m$	$\mathbf{v}_m$	$\mathbf{v}_f^{met}$	$\mathbf{v}_f^{sil}$

(melting and freezing) of metal and silicates can occur and are quantified by the melting rates Γ^{met} and Γ^{sil} (in kg m^{-3} s^{-1}). For simplicity we neglect the density difference between solid and liquid states of both the metal $\left(\rho_m^{met} = \rho_f^{met} \equiv \rho^{met}\right)$ and the silicates $\left(\rho_m^{sil} = \rho_f^{sil} \equiv \rho^{sil}\right)$, and the thermal expansion. This is justified by the one order of magnitude larger density difference between the two components. We assume identical viscosities of the solid components $\left(\mu_m^{sil} = \mu_m^{met} \equiv \mu_m\right)$, the liquid metal and liquid silicate viscosities being μ_f^{met} and μ_f^{sil}, both negligible with respect to μ_m. Table 3 summarizes this setup that generalizes the approach used in Šrámek et al. (2010).

Since the melting temperature of the silicate component is higher than that of metal, all four constituents cannot coexist, as we assume univariant melting of each component. At most three species can be in local equilibrium: either solid mixture and molten metal, or solid silicates and molten mixture.

3.1.1. Segregation of molten metal

The conservation of silicates and metal in both phases is expressed by a set of four conservation equations with mass sources on the right-hand sides due to melting/freezing,

$$\frac{\partial \phi_m^{sil}}{\partial t} + \mathbf{\nabla} \cdot \left(\phi_m^{sil} \mathbf{v}_m\right) = -\frac{\Gamma^{sil}}{\rho^{sil}}, \tag{9}$$

$$\frac{\partial \phi_m^{met}}{\partial t} + \mathbf{\nabla} \cdot \left(\phi_m^{met} \mathbf{v}_m\right) = -\frac{\Gamma^{met}}{\rho^{met}}, \tag{10}$$

$$\frac{\partial \phi_f^{met}}{\partial t} + \mathbf{\nabla} \cdot \left(\phi_f^{met} \mathbf{v}_f^{met}\right) = \frac{\Gamma^{met}}{\rho^{met}}, \tag{11}$$

$$\frac{\partial \phi_f^{sil}}{\partial t} + \mathbf{\nabla} \cdot \left(\phi_f^{sil} \mathbf{v}_f^{sil}\right) = \frac{\Gamma^{sil}}{\rho^{sil}}. \tag{12}$$

The molten silicates should be lighter that the solid silicates. However, as their density difference is more than 10 times smaller that between silicates and metal, we neglect this difference. The molten silicates remain therefore stationary relative to the solid matrix and $\mathbf{v}_f^{sil} = \mathbf{v}_m$ and, accordingly, we do not partition the moderately incompatible Al between the solid and molten silicates. We define the solid volume fraction $\phi_m \equiv \phi_m^{sil} + \phi_m^{met}$ and the liquid volume fraction $\phi_f \equiv \phi_f^{met} + \phi_f^{sil}$ (see Table 3).

The momentum equation for the entire solid–melt mixture is

$$-\mathbf{\nabla}\overline{P} + \mathbf{\nabla} \cdot [\phi_m \underline{\boldsymbol{\tau}}_m] + \bar{\rho}\mathbf{g} = 0, \tag{13}$$

where inertial terms, viscous stress in the fluid phase and interfacial tension are neglected. The average pressure $\overline{P}$ and the average density $\bar{\rho}$ are

$$\overline{P} = \left(\phi_m^{sil} + \phi_m^{met}\right)P_m + \left(\phi_f^{met} + \phi_f^{sil}\right)P_f = \phi_f P_f + \phi_m P_m, \tag{14}$$

$$\bar{\rho} = \left(\phi_m^{sil} + \phi_f^{sil}\right)\rho^{sil} + \left(\phi_m^{met} + \phi_f^{met}\right)\rho^{met}. \tag{15}$$

The deviatoric stress in the solid viscous matrix is

$$\underline{\boldsymbol{\tau}}_m = \mu_m\left(\mathbf{\nabla}\mathbf{v}_m + [\mathbf{\nabla}\mathbf{v}_m]^T - \frac{2}{3}\mathbf{\nabla} \cdot \mathbf{v}_m\underline{\mathbf{I}}\right). \tag{16}$$

The separation of the liquid metal from the solid matrix is described as Darcy flow where the difference in velocities $\Delta\mathbf{v} = \mathbf{v}_m - \mathbf{v}_f^{met}$ arises from non-hydrostatic pressure gradients in the fluid according to

$$\phi_f^{met}\Delta\mathbf{v} = \frac{k\left(\phi_f^{met}\right)}{\mu_f}\left(\mathbf{\nabla}P_f - \rho^{met}\mathbf{g}\right), \tag{17}$$

where $k\left(\phi_f^{met}\right)$ is the permeability of the matrix which depends on the liquid volume fraction, and μ_f is the fluid viscosity (McKenzie, 1984; Bercovici et al., 2001). We employ the usual relationship between permeability and the interconnected volume fraction of fluid,

$$k\left(\phi_f^{met}\right) = k_0\left(\frac{\phi_f^{met} - \phi_c}{\phi_0 - \phi_c}\right)^n, \tag{18}$$

valid for a liquid metal volume fraction above the interconnectivity threshold $\left(\phi_f^{met} > \phi_c\right)$; k_0 is a coefficient proportional to the square of average grain size (Schmeling, 2000). Below this threshold the permeability is zero. At the reference porosity ϕ_0 the permeability is k_0.

The difference in pressures between the solid matrix and the liquid metal is due to the isotropic deformation of the solid and the interfacial tension; this latter contribution is non-zero even in static case, but here we neglect the interfacial tension. As shown previously (Bercovici et al., 2001),

$$P_f - P_m = K_0\frac{\mu_m}{\phi_f - \phi_c}\mathbf{\nabla} \cdot \mathbf{v}_m, \tag{19}$$

where K_0 is a geometrical factor close to 1, and we take $K_0 = 1$ from now on.

Combination of (13), (17) and (19),

$$\phi_f^{met}\Delta\mathbf{v} = \frac{k\left(\phi_f^{met}\right)}{\mu_f}\left[\mathbf{\nabla} \cdot (\phi_m\underline{\boldsymbol{\tau}}_m) + \mathbf{\nabla}\left(\frac{\mu_m\phi_m}{\phi_f - \phi_c}\mathbf{\nabla} \cdot \mathbf{v}_m\right)\right.$$
$$\left. - \left(\phi_m^{sil} + \phi_f^{sil}\right)(\rho^{met} - \rho^{sil})\mathbf{g}\right], \tag{20}$$

gives a useful relation from which pressures have been eliminated, between the liquid metal–solid mixture or liquid metal–silicate mixture separation velocity $\Delta\mathbf{v}$. Three forces enter this relation: the stresses due to shear deformation (the $\underline{\boldsymbol{\tau}}_m$ term), those due to isotropic deformation of the matrix (the $\mathbf{\nabla} \cdot \mathbf{v}_m$ term) and the buoyancy (term proportional to $\mathbf{g}$).

Eq. (20) is used to compute the separation of molten metal from the solid mixture. As liquid and solid silicates have the same density in our model, they do not separate. Notice also, that in this 1-D spherical model, no Rayleigh–Taylor instabilities ("multiphase diapirs", see Šrámek et al., 2010) can occur and therefore the silicate melt can remain trapped beneath a denser solid layer. We are not solving a specific equation for the separation of liquid metal from liquid silicates (a metal rain in a silicate melt). Such an equation would be mathematically somewhat similar to (20) but the separation would be controlled by the viscosity of liquid silicates, rather than that of the solid component μ_m and thus, would be very rapid. Our model is therefore controlled by the timescale of molten metal–solid matrix separation, while the timescales of molten metal–molten silicate separation is so rapid that we simply assume an instantaneous unmixing of the two components, and the separation of liquid silicate from solid silicate too sluggish to be taken into account.

The energy balance in the two-phase medium undergoing phase change is,

$$\overline{\rho C}\frac{\overline{D}T}{Dt} + L^{met}\Gamma^{met} + L^{sil}\Gamma^{sil} = \overline{\rho}H + \nabla \cdot (k_T \nabla T), \tag{21}$$

where L^{met} and L^{sil} are the latent heats of melting for the metal and the silicates. We assume local thermal equilibrium between the constituents, therefore a single temperature, which is reasonable for the present porous flow model. For simplicity we assumed identical specific heat for solid and liquid states of both components ($C_m^{met} = C_f^{met} \equiv C^{met}$ and $C_m^{sil} = C_f^{sil} \equiv C^{sil}$) and used the fact that $\rho^{sil}C^{sil} \approx \rho^{met}C^{met}$ (see Table 2). The substantial derivative is

$$\frac{\overline{D}}{Dt} \equiv \left(\frac{\partial}{\partial t} + \overline{\mathbf{v}} \cdot \nabla\right), \tag{22}$$

with the frame moving at the average mixture velocity

$$\overline{\mathbf{v}} = \sum_{j=1}^{4} \phi_j \mathbf{v}_j = \left(\phi_m + \phi_f^{sil}\right)\mathbf{v}_m + \phi_f^{met}\mathbf{v}_f^{met} = \mathbf{v}_m - \phi_f^{met}\Delta\mathbf{v}. \tag{23}$$

In Eq. (21) the dissipation terms (Šrámek et al., 2007) have been omitted. The segregation of the core should dissipate gravitational energy (Monteux et al., 2009) but for our small planetesimal where segregation is only partial, this effect only increases the temperature by few tens of Kelvin.

The last two equations needed are relations for the melting rates of metal and silicates Γ^{met} and Γ^{sil}. We discuss the treatment of melting later in Section 3.2.1.

3.2. Equations in spherical symmetry

We consider a spherically symmetric planetesimal which largely simplifies the equations. This is a reasonable assumption as the bodies considered here should have a near-spherical shape and an internal temperature variation dominated by the gradient along the radius. The sum of Eqs. (9)–(12) indicates a divergence-free average velocity ($\nabla \cdot \overline{\mathbf{v}} = 0$), which in spherical symmetry implies $\overline{v} = 0$, therefore

$$v_m = \phi_f^{met}\Delta v \equiv v, \tag{24}$$

where v was introduced to simplify notation.

In spherical symmetry and performing the change of variable $r \to u = r/R(t)$ introduced in Section 2.2, to rescale the radius between 0 and 1, the mass conservation Eq. (9) can be rewritten as

$$\frac{\partial \phi_m^{sil}}{\partial t} - u\frac{\dot{R}}{R}\frac{\partial \phi_m^{sil}}{\partial u} + \frac{1}{Ru^2}\frac{\partial}{\partial u}\left(u^2 \phi_m^{sil} v\right) = -\frac{\Gamma^{sil}}{\rho^{sil}}. \tag{25}$$

The remaining individual mass conservation Eqs. (10)–(12) change accordingly.

Eq. (20) in spherical symmetry with the change of variable $r \to u$ and using the permeability–porosity relationship (18) becomes

$$v = \left(\frac{\phi_f^{met} - \phi_c}{\phi_0 - \phi_c}\right)^n \left[\left(\frac{\delta}{R}\right)^2 \frac{\partial}{\partial u}\left(\frac{\phi_m[1 + \frac{4}{3}(\phi_f - \phi_c)]}{\phi_f - \phi_c}\frac{1}{u^2}\frac{\partial(u^2 v)}{\partial u}\right)\right.$$
$$\left. + 4\left(\frac{\delta}{R}\right)^2 \frac{v}{u}\frac{\partial \phi_f}{\partial u} + \left(\phi_m^{sil} + \phi_f^{sil}\right)V_b\frac{g}{g_0}\right], \tag{26}$$
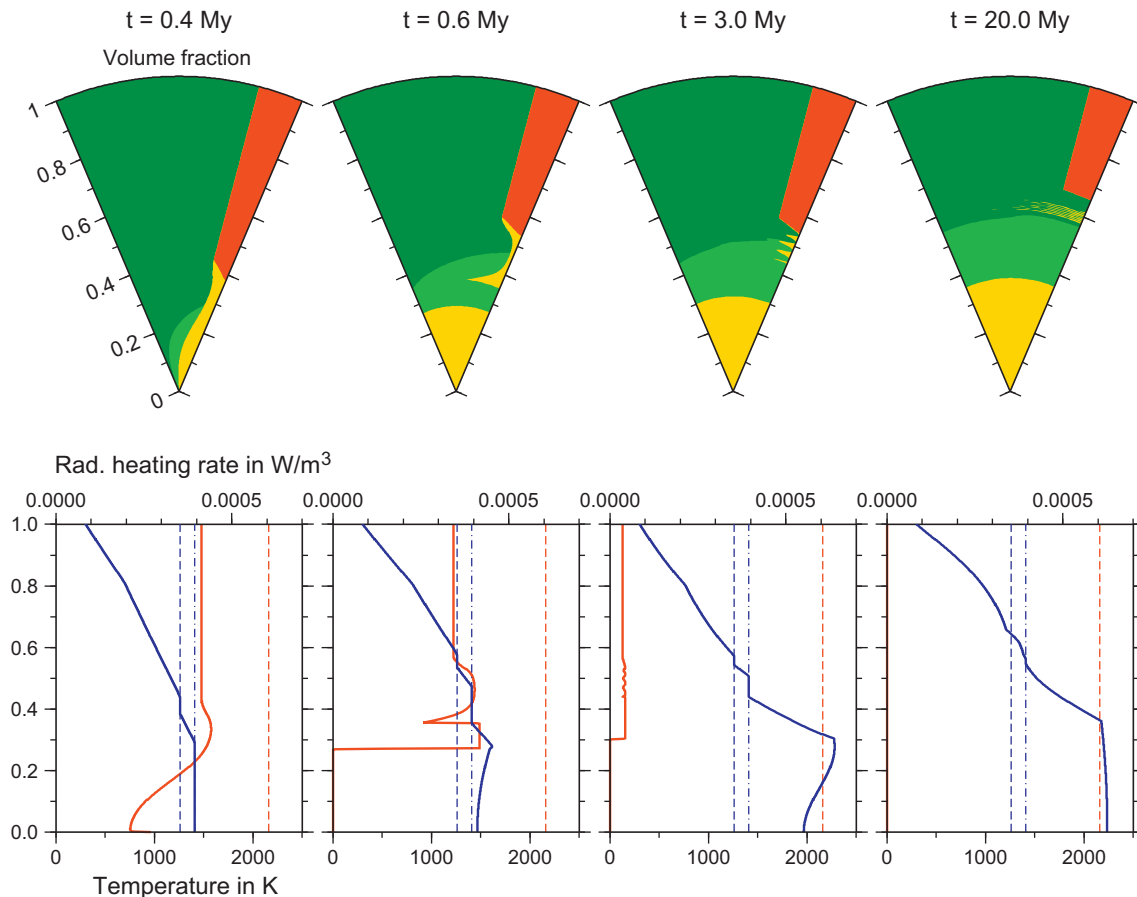

Fig. 7. Case with $t_0 = 0$, $t_a = 3$ My, $R_f = 500$ km, $\beta = 0$. Top panels: volume fractions of solid iron (red), liquid iron (yellow), solid silicate (dark green), liquid silicate (light green). Bottom panels: temperature (blue) and radiogenic heating rate (red). The melting temperature of metal and silicates are depicted by thin blue dashed and dot-dashed lines. The dashed red line shows the initial heating rate of the uniform metal–silicate mixture. (For interpretation of the references to color in this figure legend, the reader is referred to the web version of this article.)

where $\delta = \sqrt{\mu_m k_0/\mu_f}$ is the reference dimensional compaction length, $V_b = (\rho^{met} - \rho^{sil})g_0 k_0/\mu_f$ is the reference buoyancy velocity, and g_0 is the reference magnitude of gravity (i.e., the surface value for the final size body). As the average density given by (15) varies during segregation and as the planetesimal grows, the gravity

$$g(u,t) = 4\pi GR(t) \int_0^u \bar{\rho} u'^2 \mathrm{d}u' \qquad (27)$$

is a function of time and radius.

The one-dimensional energy equation is

$$\frac{\partial T}{\partial t} - u\frac{\dot{R}}{R}\frac{\partial T}{\partial u} + \frac{L^{met}\Gamma^{met} + L^{sil}\Gamma^{sil}}{\bar{\rho}\bar{C}}$$
$$= \frac{\phi_m^{sil} + \phi_f^{sil}}{1 - \phi_0}\frac{H}{\bar{C}} + \frac{1}{\bar{\rho}\bar{C}u^2}\frac{\partial}{\partial u}\left(\frac{k_T}{R^2}u^2\frac{\partial T}{\partial u}\right), \qquad (28)$$

where the ϕ-dependent factor in the internal heating term accounts for the changing proportion of the ^{26}Al-bearing silicate component. Notice that no advection term due to metal–silicate separation appears; this is a consequence of spherical symmetry, $\bar{v} = 0$ and of our assumption that the sensible heat of the two phases are equal, $\rho^{sil}C^{sil} = \rho^{met}C^{met}$.

3.2.1. Melting parameterization

To update the porosities (Eqs. (9)–(12)) and the temperature (Eq. (28)) we need to prescribe the melting rates Γ^{met} and Γ^{sil}. Like in Section 2, we implement a simple form of the enthalpy method.

We present the method for the case of iron melting at T_m^{met}. We solve (10), (11) and (28) with the melting rate identically equal to zero ($\Gamma^{met} = 0$), and thus obtain the first approximation of the new metal fractions, $\widetilde{\phi_m^{met}}$ and $\widetilde{\phi_f^{met}}$, and temperature, $\widetilde{T}$. These values are then corrected at constant enthalpy per unit volume $h = \bar{\rho}\bar{C}T + \rho^{met}L^{met}\phi_f^{met}$, to give the correct new values $\phi_m^{met} = \widetilde{\phi_m^{met}} - \delta\phi$, $\phi_f^{met} = \widetilde{\phi_f^{met}} + \delta\phi$ and $T = \widetilde{T} - \delta T$ according to the following rules:

1. If $\widetilde{T} > T_m^{met}$, the solid metal, in proportion ϕ_m^{met}, melts to decrease the temperature by $\delta T = \min\left[\widetilde{T} - T_m^{met},\ \rho^{met}L^{met}\phi_m^{met}\big/\left(\bar{\rho}\bar{C}\right)\right]$.

2. If $\widetilde{T} < T_m^{met}$, the liquid metal in proportion ϕ_f^{met} freezes to increase the temperature by $\delta T = -\min\left[T_m^{met} - \widetilde{T},\ \rho^{met}L^{met}\phi_f^{met}\big/\left(\bar{\rho}\bar{C}\right)\right]$.

The liquid metal fraction ϕ_f^{met} is then corrected by $\delta\phi = \bar{\rho}\bar{C}\delta T/(\rho^{met}L)$ and the solid metal fraction ϕ_m^{met} by $-\delta\phi$. The situation of silicate melting at T_m^{sil}, which involves ϕ_m^{sil} and ϕ_f^{sil} is treated similarly.

3.3. Numerical resolution

In the regime of solid–liquid separation, we solve the system of Eqs. (9)–(12) (in the form of Eq. (25)) and (26)–(28) by finite
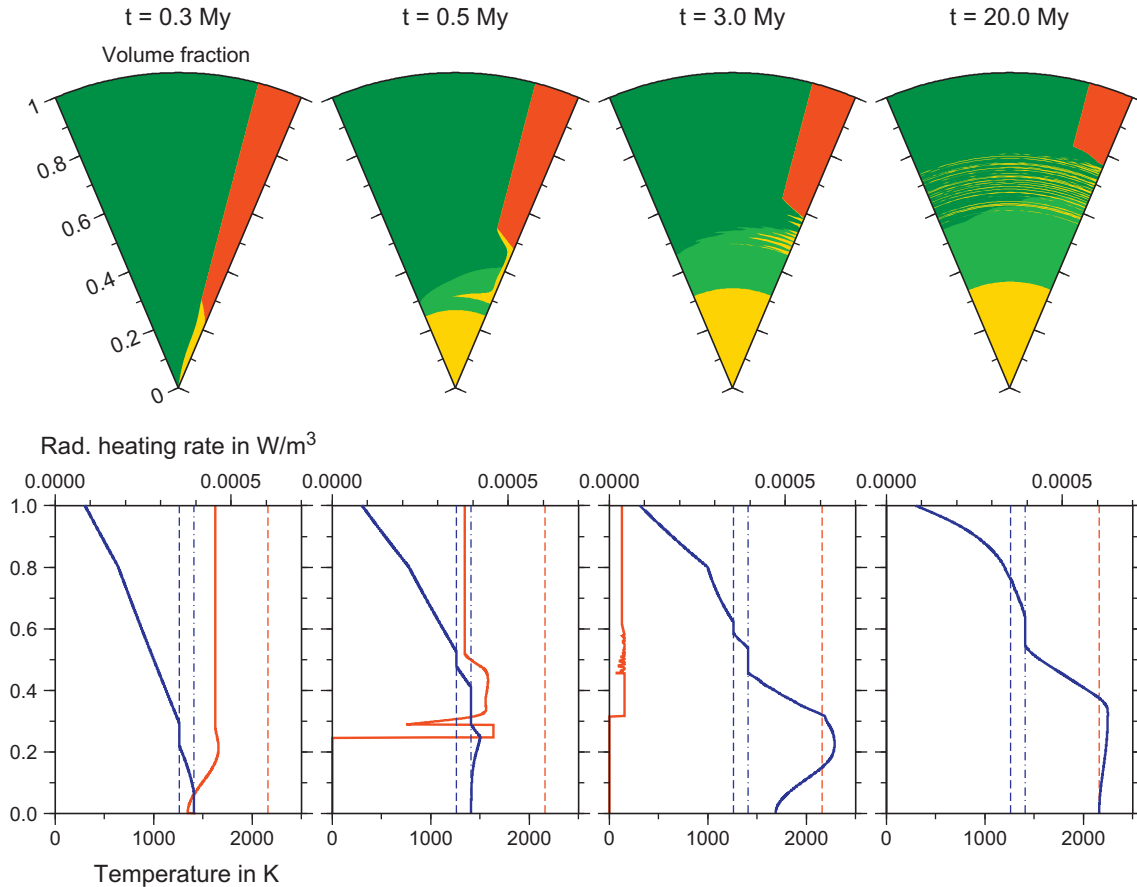

Fig. 8. Case with $t_0 = 0$, $t_{acc} = 3$ My, $R_{final} = 1000$ km, $\beta = 0$. See caption of Fig. 7 for details. (For interpretation of the references to color in this figure legend, the reader is referred to the web version of this article.)

difference schemes and use the melting parameterization of paragraph Section 3.2.1. From the knowledge of the porosities ϕ_j the numerical resolution of the coupled Eqs. (26) and (27) for velocity v and gravity g is trivial on a staggered grid with a classical tridiagonal solver; notice that the presence of a $(\phi_f - \phi_c)^n$ with $n \geqslant 2$ in front of the square parenthesis in (26) regularizes the term related to the bulk viscosity in $1/(\phi_f - \phi_c)$. From the updated velocity the new porosities and the temperature are advanced in time and corrected for melting. The whole procedure is repeated, thus time advanced.

3.4. Results of models with segregation

The segregation of planetesimals depends mostly on three parameters, the terminal size R_f, the accretion duration t_a and the exponent β controlling the evolution of the growth rate. Various simulations can be performed, but we simply present a few of them illustrating the situations introduced in the regime diagram of Fig. 4, but now with a complete dynamic multiphase modeling.

Fig. 7 depicts the radial composition of a planetesimal ($R_f = 500$ km, $t_a = 3$ My, $\beta = 0$) at various times during accretion and after accretion has stopped (the same situation without differentiation is indicated by a star symbol in Fig. 4a). The solid metal is in red, solid silicates in dark green, liquid metal in yellow, and liquid silicates in light green (top row). The time evolves from left to right, the radii are normalized but the real radii are 70, 104, 500 and 500 km from left to right.

Near the surface, the composition remains constant with 18% of metal (red) and 82% of silicates. The melting occurs from the center

and starts first with the melting of the metallic phase, then as temperature increases, of the silicate phase. The molten metal percolates through the solid matrix. When the background liquid fraction approaches zero and extraction of the remaining liquid becomes difficult, compaction waves develop that were described in many previous studies (e.g., Scott and Stevenson, 1984; Scott et al., 1986; Barcilon and Richter, 1986). When no solid phase remains, the molten metal and molten silicates separate instantaneously. Ultimately a metallic core of total volumetric fraction of 5% forms. Large outer parts of the planetesimal (71% by volume) remain undifferentiated and 24% consists of silicates that have been partially or totally molten.

The bottom row of Fig. 7 shows the temperature (thick blue line) and radiogenic heating rate sources (thick red line) as a function of radius. The melting temperatures of the metal and the silicate are shown as thin dashed and dash-dotted blue lines. The initial uniformly distributed radioactivity is shown as thin red dashed line. During core segregation the ^{26}Al is progressively transported with the silicate phase. This decreases the maximum temperature that the metallic core can reach (compare Fig. 5a with Fig. 7 at 3 My; both show the temperature profile when the peak temperature was reached in each case; the peak temperature decrease from 4124 to 2324 K). Unlike in the case without segregation, the temperature is now a non-monotonic function of radius. In addition to the temperature plateaus due to the univariant phase changes, the temperature in the metallic core decreases towards the center due to the absence of radiogenic heating. This temperature profile leads to a stably stratified core in a few million years. About 5 My after the end of accretion when the internal heat
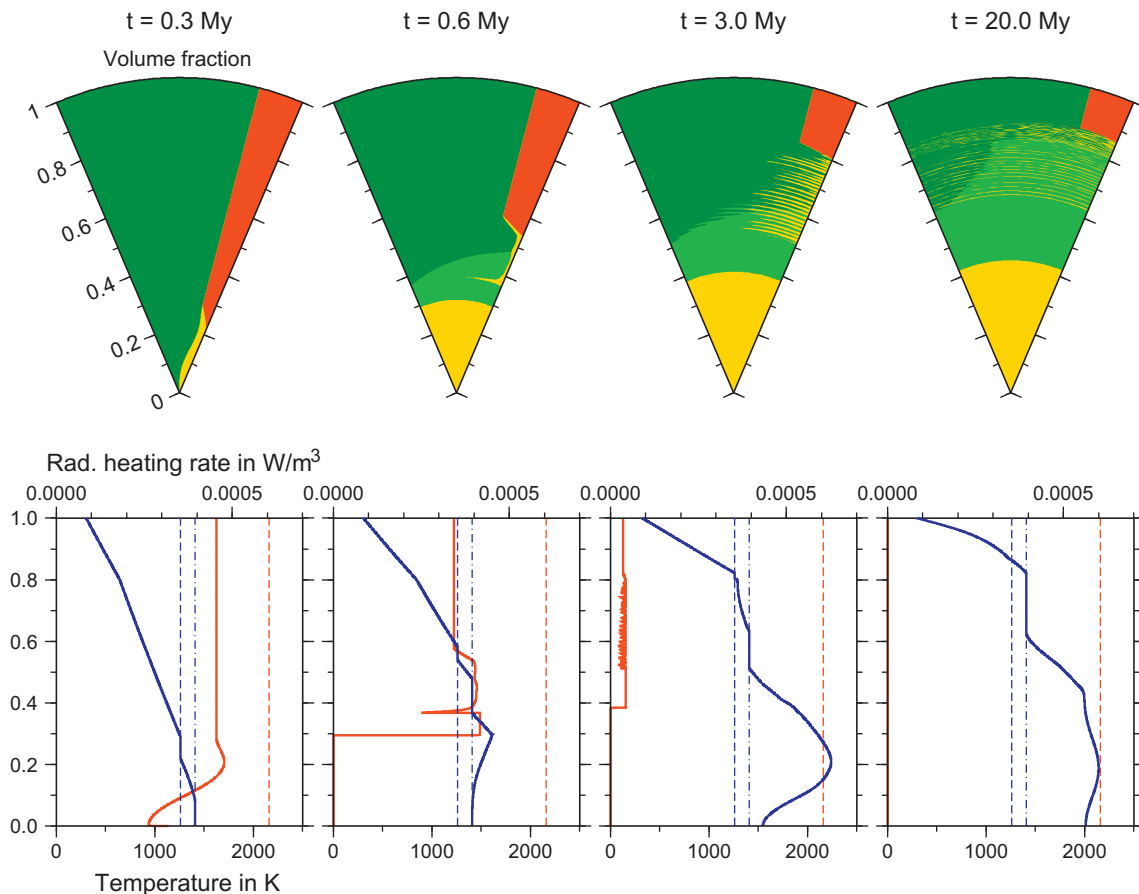

Fig. 9. Case with $t_0 = 0$, $t_a = 3$ My, $R_{final} = 1500$ km, $\beta = 0$. See caption of Fig. 7 for details. (For interpretation of the references to color in this figure legend, the reader is referred to the web version of this article.)

sources are exhausted, the internal temperature starts to decrease as the average temperature gradient in the undifferentiated and silicate-rich shells of this small object is quite large – about 6 K km^{-1} (2000 K in 330 km)

For planetesimals accreting to 1000 or 1500 km in t_a = 3 My and still with β = 0 (steady radial growth), the evolution is rather similar (see Figs. 8 and 9; these two cases correspond to the star symbols in Fig. 4b and c). The volume of the protocore now represents 4% and 7% of the total volume, and the proportion of undifferentiated outer shell decreases to 50% and 34% by volume, respectively, the rest being silicates with varying degrees of melting. The radiogenic heating rate is largest where the fraction of metal is lowest, which happens to be at the bottom of the mantle. This results in heating up the core from above and the mantle from below. After the radiogenic heating has decayed, cooling progresses from the top down, and the core remains hot longer than the mantle, which explains the temperature profile at the end of accretion (Figs. 8 and 9 at 3 My).

The planetesimal evolution is very different when the exponent β is increased: see Figs. 10 and 11 which correspond to a planetesimal reaching 1500 km in 3 My, like the case in Fig. 9, but this time with β = 1 and β = 2, respectively. The slower growth at the beginning of accretion allows the radiogenic heat to be radiated away, while the final acceleration of the accretion induces significant surface heating. When β = 1 (Fig. 10), a very limited melting occurs at the planetesimal center and in a shallow magma ocean. A further increase in β (Fig. 11) leads to melting starting only in a shallow magma ocean. In this outer zone, the segregation leads to a metal

layer that cannot sink in this 1-D simulation. In a realistic 3-D case, Rayleigh–Taylor instabilities could allow the segregation of metal in a mixed diapir/porous flow dynamics described in Šrámek et al. (2010). In larger bodies, the liberation of potential energy associated with the redistribution of mass induces significant heating by viscous and Darcy dissipation (Monteux et al., 2009). This should lead to a runaway melting of the whole planetesimal (Ricard et al., 2009).

Table 4 summarizes the results of calculations with metal–silicate segregation and lists the final volume fraction of the central metallic core as well as the volume extent of the unsegregated region that has stayed below melting at all times. For a planetesimal of terminal radius R_f = 1500 km we ran a series of cases in order to explore the effects of t_a and β, even though the outcomes can, to some extent, be predicted from the static calculations presented in Fig. 4. For an accretion time comparable to or shorter than the ^{26}Al half-life, the entire planetesimal is heated well above the silicate melting temperature. This is independent of the accretion law exponent β and results in a fully segregated core and no undifferentiated regions. If the accretion time exceeds $\sim 6 \times {}^{26}$Al half-life (4.5 My), melting, if present, is limited to small volumes. The segregated core volume is negligible and most of the planetesimal remains undifferentiated. For intermediate accretion times, e.g., $\sim 3 \times {}^{26}$Al half-life, partial differentiation of the planetesimal occurs. The location of the differentiated region depends on the accretion law exponent β, where a higher β indicates a stronger contribution of the gravitational heating by impacts, therefore possible melting and differentiation at shallow depth.

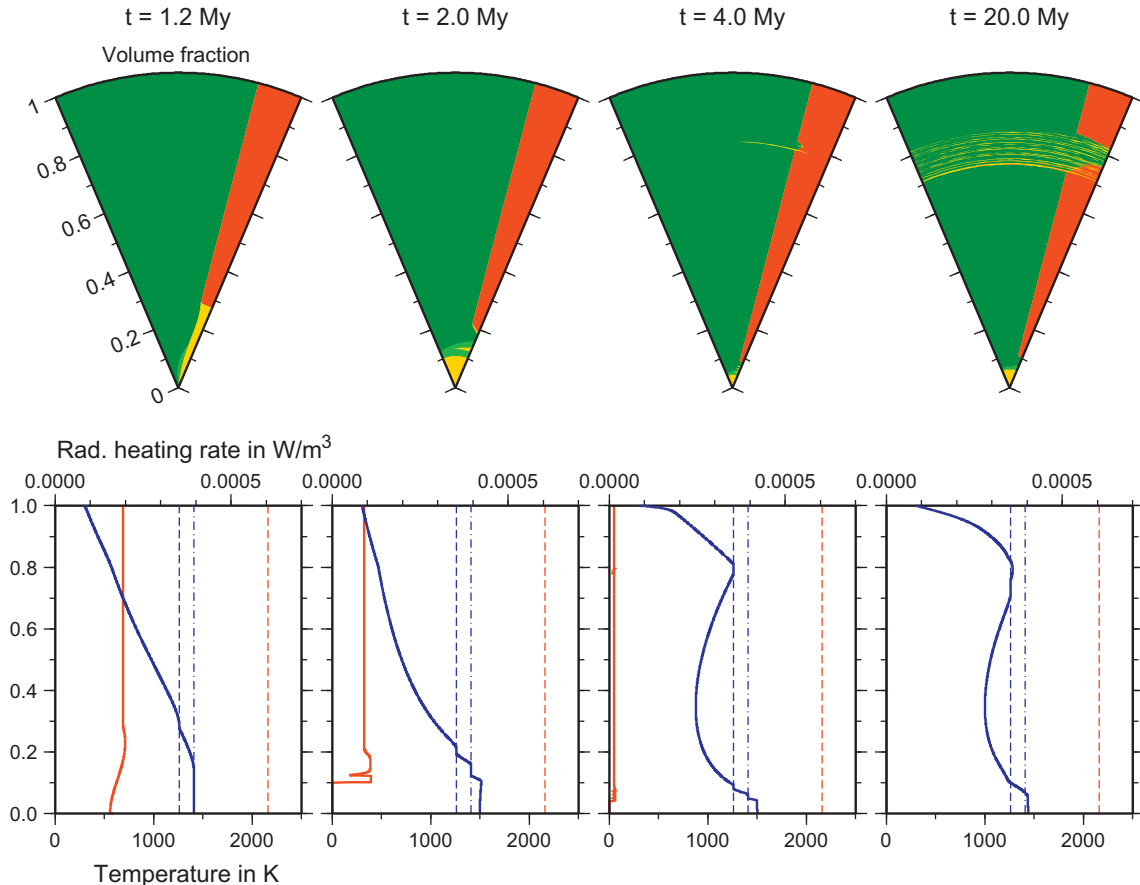**Fig. 10.** Case with t_0 = 0, t_a = 3 My, R_{final} = 1500 km, β = 1. See caption of Fig. 7 for details. (For interpretation of the references to color in this figure legend, the reader is referred to the web version of this article.)
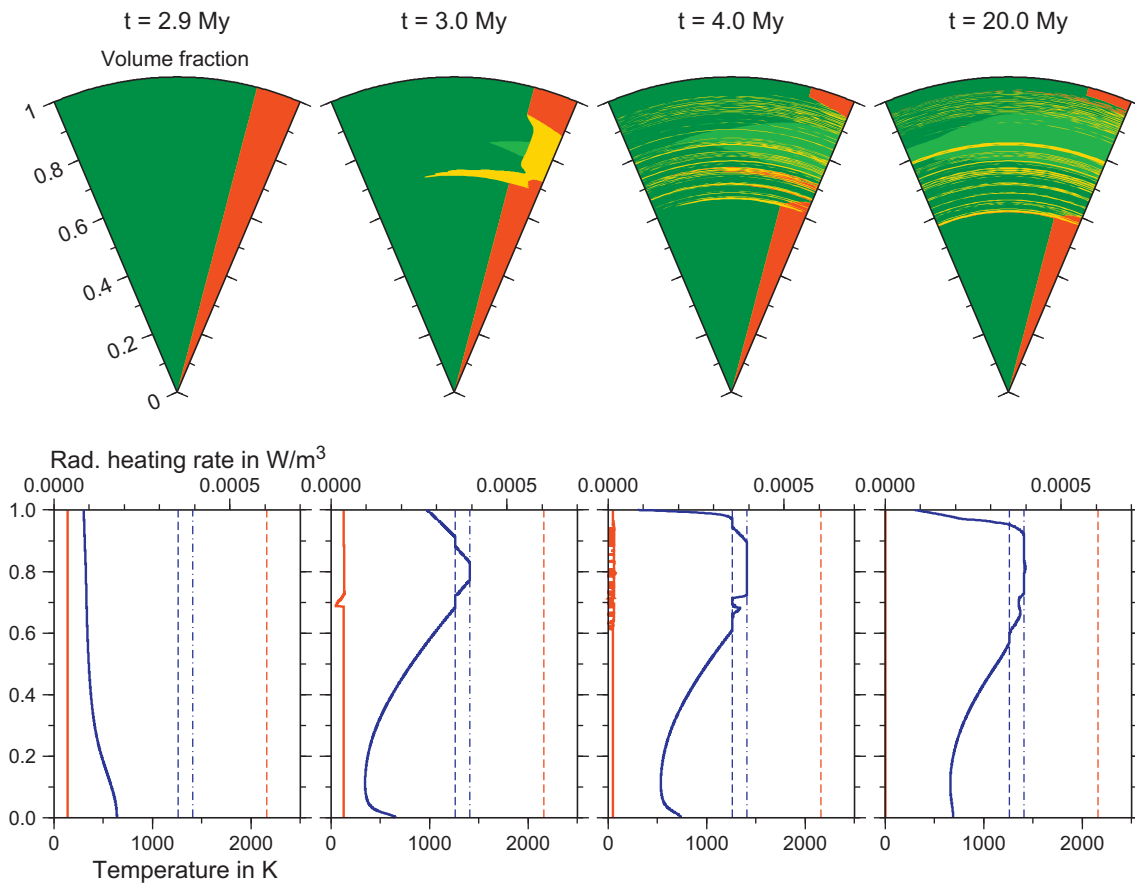
Fig. 11. Case with $t_0 = 0$, $t_a = 3$ My, $R_{final} = 1500$ km, $\beta = 2$. See caption of Fig. 7 for details. (For interpretation of the references to color in this figure legend, the reader is referred to the web version of this article.)

Table 4
Results of calculations with metal–silicate segregation. The maximum possible core volume fraction 18% was reached in some cases. In cases denoted with an asterisk, the total unsegregated volume fraction is contributed by the cold surface shell plus an unsegregated shell at depth with a partially segregated region in between. Segregated metallic shallow layers that have not reached the center are not included in the core volume. All cases assume that accretion started immediately after element synthesis $t_0 = 0$.

R_f in km	t_a in My	Exponent β	Core vol.%	Unseg. vol.%
500	3	0	5	71
1000	3	0	4	50
1500	1	0	~18	2
1500	1	1	~18	2
1500	1	2	~18	0
1500	3	0	7	34
1500	3	1	<1	77 (42 + 35)*
1500	3	2	0	26 (8 + 18)*
1500	5	0	1	90
1500	5	1	≪1	~100
1500	5	2	0	70 (33 + 37)*

4. Discussion and conclusion

The abundance of radioactive short period elements seems largely enough to explain the melting of planetesimals a few million years after accretion, as contended Yoshino et al. (2003). Simple back of the envelope estimates would suggest that temperature of order $H(0)\tau_{1/2}/C$, in excess of 5000 K, could be reached except in a cold boundary layer of thickness $\pi\sqrt{\kappa\tau_{1/2}}$ (~20 km). However,

the maximum temperature that can be attained and the extent of the melting can be largely different from these values when the effect of accretion over a finite time interval is considered (i.e., as opposed to an instantaneous planetary formation).

Until the planetesimal radius reaches the characteristic thermal diffusion scale of ~20 km, the temperature remains very low and close to that of the nebula. Then, the blanketing effect of newly accreted material thermally protects the deepest parts of the growing planet from cooling. As the radioactivity is delivered during a time of order $\tau_{1/2}$ when the planetesimal has a radius of order $R(0) + \dot{R}(\tau_{1/2})\tau_{1/2}$, the effectively heated central region and therefore the potential protocore has also a radius of the same order. In the likely case where $\dot{R} \propto R^\beta$ with $\beta = 2$, the planetesimal growth rate is very slow at the beginning of accretion. Even in the case where planetary embryos as large as 1500 km in radius are formed in 5 My, only a very small volume can be melted by radiogenic heating. Radiogenic heating due to ^{26}Al is therefore only significant if large planetesimals (i.e., $R \gg 20$ km) are formed within a couple of ^{26}Al half-lives.

The initial radioactive heating is followed by surface heating due to bombardment by meteorites. The fact that the impactors themselves are hot and deliver both thermal and gravitational energies does not play a significant role in the energy budget of small planetesimals ($R < 1000$ km). Impactors are by definition smaller and thus colder than the impacted bodies, and gravitational energy becomes significant only for more massive bodies. The radiative dissipation of energy in the absence of atmosphere is very efficient to remove this accretion energy unless the accretion energy is buried at depth – by penetration of the impactors,

by mixing of the superficial layers during the impact, or most efficiently by shock energy release at depth. This source of energy is efficient for large planetesimals ($R \gtrsim 1000$ km). It is the only cause of melting for planetesimals that reach this size in more than a couple of ^{26}Al half-lives.

When metal–silicate differentiation is taken into account, the temperature reached in the center of planetesimals is buffered as the ^{26}Al sources remaining in the lighter silicates are transported closer to the surface. The opposite effect (not considered in this paper) would occur for the longer period ^{60}Fe sources that would move preferentially to the protocore and would increase the central temperature.

Overall, the results of our modeling show that the thermal evolution and final degree of differentiation of early planetesimals depend on all of the following variables: the final planetesimal size, the duration of accretion, the form of the accretion law as well as the start time of accretion (relative to the time of element synthesis). Within the reasonable parameter values that we considered, the outcomes range from undifferentiated cold bodies to fully differentiated, totally molten planetesimals. This variability can be attributed to three factors – first, the half-life of radiogenic heat sources is of the same order as the accretion time; second, the planetesimal evolves from a seed smaller than the thermal diffusion length but grows to a size well above this length scale; and third, the power of gravitational heating by impactors increases with increasing planetesimal size, decreasing accretion time and increasing exponent β in the relation for the accretion rate (i.e., with more accelerated accretion). If we did not consider the gravitational heating by impactors, the problem would be greatly simplified. The question of maximum interior temperature would, in principle, boil down to calculating the time when the planetesimal size exceeds the thermal diffusion length, relative to the half-life of radiogenic sources. While bringing more realistic physics into the analysis, the inclusion of gravitational heating which is the strongest towards the end of accretion, complicates the simple heating vs. diffusion picture.

Various groups of meteorites have been identified, based on their bulk compositions and textures. The main division is between chondrites which experienced heating but not melting, and non-chondrites that experienced melting and differentiation; the latter include silicate-rich primitive achondrites, and differentiated metal-poor achondrites, stony irons and iron meteorites (e.g., Krot et al., 2003). Meteorites exhibit a large variation in metal content and degree of differentiation. Petrological, mineralogical, chemical and isotopic analyses of meteorite groups suggest the existence of 100–150 distinct parent bodies, even though it proves difficult to conclusively link most asteroids with particular meteorite groups (Burbine et al., 2002). A distinct parent body is generally invoked for each different meteorite group and for every ungrouped meteorite. As we have shown, it is possible to accrete a planetesimal with a differentiated protocore, an undifferentiated outer shell and a partially segregated intermediate region (Figs. 7–11). In terms of metallic proportions, it is conceivable that meteorites belonging to several different groups may originate from the same parent body. For example, the protocore may yield an iron meteorite, a pallasite (stony iron) may originate from the core–mantle boundary region or, more likely in a statistical sense, the partially segregated shell, while a chondrite may come from the undifferentiated outer shell. This suggestion offers an interesting motivation for a more detailed study that should assess the geochemical plausibility of such a scenario. Elkins-Tanton et al. (2011) also discussed the possibility of chondrites being samples from a partly differentiated planetesimal, even though their model assumes a simple instantaneous accretion.

Paleomagnetic analyses of meteoritic samples indicate that parent bodies of some meteorites, in particular angrites (basaltic achondrites) and the Allende CV chondrite, possessed an early internally generated magnetic field, operating within few million years of Solar System formation (Weiss et al., 2008, 2010). The ability for the core to produce a magnetic field depend largely on its modified Rayleigh number

$$Ra_q^* = \frac{\alpha g q}{\rho C \Omega^3 D^2}, \tag{29}$$

where q and g are the heat flux and the gravity at the core-mantle boundary, D the core radius and Ω the rotation rate of the planet (Christensen and Aubert, 2006; Aubert et al., 2009). The gravity g being proportional to the radius of the core D, g/D^2 is larger in small planetesimals than in the Earth. The protocore–mantle boundary heat flux $q \sim 30$ mW m^{-2}, calculated from a temperature gradient of ~ 10 K km^{-1} (see Fig. 7 at 20 My) is comparable to that extracted from the Earth's core at present day. Therefore at similar (or smaller) rotation rates, the protocore modified Rayleigh numbers of planetesimals during differentiation were larger than that of the Earth. They most probably had intense magnetic fields during accretion through their final core freezing, which for objects of 500–1500 km takes hundreds of million years. These magnetic fields should be recorded in the planetesimal silicates that for a large proportion have crossed the Curie temperature of their magnetic components during that time.

Acknowledgments

References

Aubert, J., Labrosse, S., Poitou, C., 2009. Modelling the palaeo-evolution of the geodynamo. Geophys. J. Int. 179 (3), 1414–1428.

Bagdassarov, N., Golabek, G.J., Solferino, G., Schmidt, M.W., 2009. Constraints on the Fe–S melt connectivity in mantle silicates from electrical impedance measurements. Phys. Earth Planet. Int. 177 (3–4), 139–146.

Barcilon, V., Richter, F.M., 1986. Nonlinear waves in compacting media. J. Fluid Mech. 164, 429–448.

Bercovici, D., Ricard, Y., Schubert, G., 2001. A two-phase model for compaction and damage. Part 1: General theory. J. Geophys. Res. 106 (B5), 8887–8906.

Burbine, T.H., McCoy, T.J., Meibom, A., Gladman, B., Keil, K., 2002. Meteoritic parent bodies: Their number and identification. In: Bottke, W., Cellino, A., Paolicchi, P., Binzel, R.P. (Eds.), Asteroids III. University of Arizona Press, pp. 653–667.

Carslaw, H.S., Jaeger, J.C., 1959. Conduction of Heat in Solids, second ed. Oxford University Press.

Castillo-Rogez, J., Johnson, T.V., Lee, M.H., Turner, N.J., Matson, D.L., Lunine, J., 2009. ^{26}Al decay: Heat production and a revised age for Iapetus. Icarus 204 (2), 658–662.

Christensen, U.R., Aubert, J., 2006. Scaling properties of convection-driven dynamos in rotating spherical shells and application to planetary magnetic fields. Geophys. J. Int. 166 (1), 97–114.

Cohen, B.A., Coker, R.F., 2000. Modeling of liquid water on CM meteorite parent bodies and implications for amino acid racemization. Icarus 145 (2), 369–381.

Croft, S.K., 1982. A first-order estimate of shock heating and vaporization in oceanic impacts. Geol. Soc. Am. Spec. Paper 190, 143–152.

Cuzzi, J.N., Hogan, R.C., Shariff, K., 2008. Toward planetesimals: Dense chondrule clumps in the protoplanetary nebula. Astrophys. J. 687 (2), 1432–1447.

Elkins-Tanton, L.T., Weiss, B.P., Zuber, M.T., 2011. Chondrites as samples of differentiated planetesimals. Earth Planet. Sci. Lett. 305 (1–2), 1–10.

Fei, Y., Bertka, C.M., Finger, L.W., 1997. High-pressure iron–sulfur compound, Fe$_3$S$_2$, and melting relations in the Fe–FeS system. Science 275 (5306), 1621–1623.

Ghosh, A., McSween, H.Y., 1998. A thermal model for the differentiation of asteroid 4 Vesta, based on radiogenic heating. Icarus 134 (2), 187–206.

Golabek, G.J., Schmeling, H., Tackley, P.J., 2008. Earth's core formation aided by flow channelling instabilities induced by iron diapirs. Earth Planet. Sci. Lett. 271 (1–4), 24–33.

Huss, G.R., Meyer, B.S., Srinivasan, G., Goswami, J.N., Sahijpal, S., 2009. Stellar sources of the short-lived radionuclides in the early Solar System. Geochim. Cosmochim. Acta 73 (17), 4922–4945.

Ichikawa, H., Labrosse, S., Kurita, K., 2010. Direct numerical simulation of an iron rain in the magma ocean. J. Geophys. Res. 115 (B1), B01404.

Johansen, A., Oishi, J.S., Low, M.-M.M., Klahr, H., Henning, T., Youdin, A., 2007. Rapid planetesimal formation in turbulent circumstellar disks. Nature 448 (7157), 1022–1025.

Jurewicz, A.J.G., Mittlefehldt, D.W., Jones, J.H., 1993. Experimental partial melting of the Allende (CV) and Murchison (CM) chondrites and the origin of asteroidal basalts. Geochim. Cosmochim. Acta 57 (9), 2123–2139.

King, C., Olson, P., 2011. Heat partitioning in metal–silicate plumes during Earth differentiation. Earth Planet. Sci. Lett. 304 (3–4), 577–586.

Kleine, T. et al., 2009. Hf–W chronology of the accretion and early evolution of asteroids and terrestrial planets. Geochim. Cosmochim. Acta 73 (17), 5150–5188.

Kleine, T., Münker, C., Mezger, K., Palme, H., 2002. Rapid accretion and early core formation on asteroids and the terrestrial planets from Hf–W chronometry. Nature 418 (6901), 952–955.

Kojitani, H., Akaogi, M., 1995. Measurement of heat of fusion of model basalt in the system diopside–forsterite–anorthite. Geophys. Res. Lett. 22 (17), 2329–2332.

Kokubo, E., Ida, S., 1996. On runaway growth of planetesimals. Icarus 123 (1), 180–191.

Kokubo, E., Ida, S., 2000. Formation of protoplanets from planetesimals in the solar nebula. Icarus 143 (1), 15–27.

Kortenkamp, S.J., Kokubo, E., Weidenschilling, S., 2000. Formation of planetary embryos. In: Canup, R.M., Righter, K. (Eds.), Origin of the Earth and Moon. The University of Arizona Press, Tucson, pp. 85–100.

Krot, A.N., Keil, K., Scott, E.R.D., Goodrich, C.A., Weisberg, M.K., 2003. Classification of meteorites. In: Holland, H.D., Turekian, K.K. (Eds.), Meteorites, Comets, and Planets, Treatise on Geochemistry, vol. 1. Elsevier Scientific Publishing Company, Oxford, pp. 83–128 (Chapter 1.05).

Lodders, K., Fegley, B., 1998. The Planetary Scientist's Companion. Oxford University Press, New York, USA.

Matsui, T., Abe, Y., 1986. Formation of a 'magma ocean' on the terrestrial planets due to the blanketing effect of an impact-induced atmosphere. Earth Moon Planets 34 (3), 223–230.

McKenzie, D., 1984. The generation and compaction of partially molten rock. J. Petrol. 25 (3), 713–765.

Melosh, H.J., 1996. Impact Cratering: A Geologic Process. Oxford University Press, New York.

Merk, R., Breuer, D., Spohn, T., 2002. Numerical modeling of ^{26}Al-induced radioactive melting of asteroids considering accretion. Icarus 159 (1), 183–191.

Minarik, W.G., Ryerson, F.J., Watson, E.B., 1996. Textural entrapment of core-forming melts. Science 272 (5261), 530–533.

Monteux, J., Ricard, Y., Coltice, N., Dubuffet, F., Ulvrová, M., 2009. A model of metal–silicate separation on growing planets. Earth Planet. Sci. Lett. 287 (3–4), 353–362.

Morbidelli, A., Bottke, W.F., Nesvorný, D., Levison, H.F., 2009. Asteroids were born big. Icarus 204 (2), 558–573.

O'Keefe, J.D., Ahrens, T.J., 1977. Impact-induced energy partitioning, melting, and vaporization on terrestrial planets. In: Merril, R.B. (Ed.), Lunar Planet. Sci. Conf. Proc., 8, 3357–3374.

Ouellette, N., Desch, S., Bizzarro, M., Boss, A., Ciesla, F., Meyer, B., 2009. Injection mechanisms of short-lived radionuclides and their homogenization. Geochim. Cosmochim. Acta 73 (17), 4946–4962.

Quitté, G., Markowski, A., Latkoczy, C., Gabriel, A., Pack, A., 2010. Iron-60 heterogeneity and incomplete isotope mixing in the early Solar System. Astrophys. J. 720 (2), 1215–1224.

Ricard, Y., Šrámek, O., Dubuffet, F., 2009. A multi-phase model of runaway core–mantle segregation in planetary embryos. Earth Planet. Sci. Lett. 284 (1–2), 144–150.

Roberts, J.J., Kinney, J.H., Siebert, J., Ryerson, F.J., 2007. Fe–Ni–S melt permeability in olivine: Implications for planetary core formation. Geophys. Res. Lett. 34 (14), L14306.

Rubie, D.C., Nimmo, F., Melosh, H.J., 2007. Formation of Earth's core. In: Gerald, S., Stevenson, D.J. (Eds.), Evolution of the Earth, Treatise on Geophysics, vol. 9. Elsevier Scientific Publishing Company, New York, pp. 51–90 (Chapter 9.03).

Rugel, G. et al., 2009. New measurement of the ^{60}Fe half-life. Phys. Rev. Lett. 103 (7), 072502-1–072502-4.

Ruzicka, A., Snyder, G.A., Taylor, L.A., 1997. Vesta as the howardite, eucrite and diogenite parent body: Implications for the size of a core and for large-scale differentiation. Meteorit. Planet. Sci. 32 (6), 825–840.

Samuel, H., Tackley, P.J., 2008. Dynamics of core formation and equilibrium by negative diapirism. Geochem. Geophys. Geosyst. 9 (6), Q06011-1–Q06011-15.

Schmeling, H., 2000. Partial melting and melt segregation in a convecting mantle. In: Bagdassarov, N., Laporte, D., Thompson, A.B. (Eds.), Physics and Chemistry of Partially Molten Rocks, Petrology and Structural Geology, vol. 11. Kluwer Academic Publishers, Dordrecht, pp. 141–178 (Chapter 5).

Scott, E., Krot, A., 2003. Chondrites and their components. In: Holland, H.D., Turekian, K.K. (Eds.), Meteorites, Comets, and Planets, Treatise on Geochemistry, vol. 1. Elsevier Scientific Publishing Company, Oxford, pp. 143–200 (Chapter 1.07).

Scott, D.R., Stevenson, D.J., 1984. Magma solitons. Geophys. Res. Lett. 11 (11), 1161–1164.

Scott, D.R., Stevenson, D.J., Whitehead Jr., J.A., 1986. Observations of solitary waves in a viscously deformable pipe. Nature 319 (6056), 759–761.

Senshu, H., Kuramoto, K., Matsui, T., 2002. Thermal evolution of a growing Mars. J. Geophys. Res. 107 (E12), 5118.

Shannon, M.C., Agee, C.B., 1996. High pressure constraints on percolative core formation. Geophys. Res. Lett. 23 (20), 2717–2720.

Smither, C.L., Ahrens, T.J., 1991. Melting, vaporization, and energy partitioning for impacts on asteroidal and planetary objects. In: Harris, A.W., Bowell, E. (Eds.), Asteroids, Comets, and Meteors. Lunar and Planetary Institute, Houston, pp. 561–564.

Solomon, S.C., 1979. Formation, history and energetics of cores in the terrestrial planets. Phys. Earth Planet. Int. 19 (2), 168–182.

Šrámek, O., Ricard, Y., Bercovici, D., 2007. Simultaneous melting and compaction in deformable two-phase media. Geophys. J. Int. 168 (3), 964–982.

Šrámek, O., Ricard, Y., Dubuffet, F., 2010. A multiphase model of core formation. Geophys. J. Int. 181 (1), 198–220.

Stevenson, D.J., 1981. Models of the Earth's core. Science 214 (4521), 611–619.

Stevenson, D.J., 1990. Fluid dynamics of core formation. In: Newsom, H.E., Jones, J.H. (Eds.), Origin of the Earth. Oxford University Press, New York, pp. 231–249.

Takahashi, E., 1983. Melting of a Yamato L3 chondrite (Y-74191) up to 30 kbar. In: Proc. NIPR Symp. Antarctic Meteorites, vol. 8, pp. 168–180.

Taylor, G.J., 1992. Core formation in asteroids. J. Geophys. Res. 97 (E9), 14717–14726.

Terasaki, H., Frost, D.J., Rubie, D.C., Langenhorst, F., 2005. The effect of oxygen and sulphur on the dihedral angle between Fe–O–S melt and silicate minerals at high pressure: Implications for martian core formation. Earth Planet. Sci. Lett. 232 (3–4), 379–393.

Terasaki, H., Frost, D.J., Rubie, D.C., Langenhorst, F., 2008. Pecolative core formation in planetesimals. Earth Planet. Sci. Lett. 273, 132–137.

von Bargen, N., Waff, H.S., 1986. Permeabilities, interfacial areas and curvatures of partially molten systems: Results of numerical computation of equilibrium microstructures. J. Geophys. Res. 91 (B9), 9261–9276.

Walker, D., Agee, C.B., 1988. Ureilite compaction. Meteoritics 23 (1), 81–91.

Walte, N.P., Becker, J.K., Bons, P.D., Rubie, D.C., Frost, D.J., 2007. Liquid-distribution and attainment of textural equilibrium in a partially-molten crystalline system with a high-dihedral-angle liquid phase. Earth Planet. Sci. Lett. 262 (3–4), 517–532.

Walter, M.J., Tronnes, R.G., 2004. Early Earth differentiation. Earth Planet. Sci. Lett. 225 (3–4), 253–269.

Weidenschilling, S.J., Spaute, D., Davis, D.R., Marzari, F., Ohtsuki, K., 1997. Accretional evolution of a planetesimal swarm. Icarus 128 (2), 429–455.

Weiss, B.P., Berdahl, J.S., Elkins-Tanton, L., Stanley, S., Lima, E.A., Carporzen, L., 2008. Magnetism on the angrite parent body and the early differentiation of planetesimals. Science 322 (5902), 713–716.

Weiss, B., Gattacceca, J., Stanley, S., Rochette, P., Christensen, U., 2010. Paleomagnetic records of meteorites and early planetesimal differentiation. Space Sci. Rev. 152 (1), 341–390.

Wetherill, G.W., Stewart, G.R., 1993. Formation of planetary embryos: Effects of fragmentation, low relative velocity, and independent variation of eccentricity and inclination. Icarus 106 (1), 190–209.

Yin, Q.Z., Jacobsen, S.B., Yamashita, K., Blichert-Toft, J., Télouk, P., Albarède, F., 2002. A short timescale for terrestrial planet formation from Hf–W chronometry of meteorites. Nature 418 (6901), 949–952.

Yoshino, T., Walter, M.J., Katsura, T., 2003. Core formation in planetisimals triggered by permeable flow. Nature 422 (6928), 154–157.

Yoshino, T., Walter, M.J., Katsura, T., 2004. Connectivity of molten Fe alloy in peridotite based on in situ electrical conductivity measurements: Implications for core formation in terrestrial planets. Earth Planet. Sci. Lett. 222 (2), 501–516.